RSC Advances

PAPER

View Article Online
View Journal | View Issue

Cite this: *RSC Adv.*, 2026, **16**, 30614

Structure–biological activity relationships in a zinc(II) pyrazole halide complex $[ZnCl_2(\eta^1\text{-}4BrPz)_2]$ *via* noncovalent interactions, molecular docking, and antimicrobial studies

Houyem Khlifi,[a] Naoufel Ben Hamadi,[b] Noureddine Mhadhbi, *[ac] Antonio Sánchez-Coronilla, [d] Khaled Hamden, [e] Ahlem Guesmi,[b] Lotfi Khezami,[b] Hajir Wahbi[f] and Houcine Naïli *[a]

A zinc-based pyrazole halide, $[ZnCl_2(\eta^1\text{-}4BrPz)_2]$ (4BrPz = $C_3H_3BrN_2$ = 4-Bromopyrazole) was synthesized and characterized by X-ray diffraction, IR spectroscopy, and Hirshfeld surface analysis. The compound crystallizes in a monoclinic system with two non-equivalent Zn(II) environments stabilized by halogen–halogen and π-interactions. DFT, ELF, and NCI analyses highlight the key role of Br···Br, Br···Cl, π-stacking, and hydrogen-bonding contacts in stabilizing the structure. Thermal studies (TGA/DSC) confirm good stability and a well-defined decomposition pathway. Molecular docking and *in silico* ADME predictions (SwissADME) were performed to evaluate the pharmacokinetic profile and biological potential of the compound, revealing favorable drug-likeness and strong binding affinity toward DNA gyrase and chitin synthase. *In vitro* tests reveal moderate, concentration-dependent antibacterial activity against eight pathogenic strains, with inhibition zones increasing from 3.9–6.3 mm at 0.5 μg mL^{-1} to 14.7–16.8 mm at 2 μg mL^{-1}. *Pseudomonas aeruginosa* and *Micrococcus luteus* were the most sensitive, while *Bacillus cereus* and *Salmonella typhi* were less affected. The tested compound $[ZnCl_2(\eta^1\text{-}4BrPz)_2]$ exhibited dose-dependent antibacterial activity against all evaluated strains, with MIC values ranging from 0.45 to 2.10 μg mL^{-1} and MBC values from 0.87 to 3.74 μg mL^{-1}. In comparison, the free ligand (4BrP) showed considerably higher MIC (2.89–7.84 μg mL^{-1}) and MBC (11.7–19.76 μg mL^{-1}) values, indicating much weaker antibacterial activity. The strongest activity of the complex was observed against *Escherichia coli* and *Bacillus cereus*, while *Salmonella typhi* and *Pseudomonas aeruginosa* were less sensitive. MBC/MIC ratios for the complex were below 4 for all strains, confirming a bactericidal effect as compared to 4BrP. These results identify $[ZnCl_2(\eta^1\text{-}4BrPz)_2]$ as a structurally robust and biologically promising zinc complex for future antimicrobial development.

Received 8th February 2026
Accepted 6th April 2026

DOI: 10.1039/d6ra01123c

rsc.li/rsc-advances

1 Introduction

Metal–organic halide compounds, distinguished by their hybrid architectures integrating metal centers with organic ligands, have attracted substantial scientific interest due to their exceptional structural, electronic, and optical properties[1–4] These compounds, positioned at the interface of organic and inorganic chemistry, offer tunable functionalities through a broad selection of metal, halide, and ligand combinations, enabling their application in catalysis,[5,6] photovoltaics,[7,8] optoelectronics,[9–11] and sensing technologies.[12] The structural versatility inherent to metal–organic halides facilitates the precise modulation of their physicochemical properties, establishing them as promising candidates for next-generation functional materials.[13–15] Their relevance has grown markedly as the demand intensifies for systems that combine structural stability with adaptable performance characteristics.[2,16,17] Although recent advances have improved synthetic accessibility and functionalization techniques, knowledge gaps persist regarding the stability and photophysical behavior of specific compositions, particularly those involving unconventional halogenated ligands

[a]*Laboratory Physical-Chemistry of the Solid State, Department of Chemistry, Faculty of Sciences of Sfax, University of Sfax, B. P. 1171, Sfax 3000, Tunisia. E-mail: noureddine2901@yahoo.fr; houcine_naili@yahoo.com*

[b]*Chemistry Department, College of Science, Imam Mohammad Ibn Saud Islamic University (IMSIU), P.O. Box 5701, Riyadh 11432, Saudi Arabia*

[c]*University of Monastir, Preparatory Institute for Engineering Studies of Monastir, 5019 Monastir, Tunisia*

[d]*Departamento de Química Física, Facultad de Farmacia, Universidad de Sevilla, E-41012 Sevilla, Spain*

[e]*Laboratory of Bioresources: Integrative Biology and Exploiting, Higher Institute of Biotechnology of Monastir, University of Monastir, Tunisia*

[f]*Department of Chemistry, College of Science, Northern Border University, Arar, Saudi Arabia*

and underexplored metal centers such as zinc.[18] In this context, the zinc-based compound $[ZnCl_2(\eta^1\text{-}4BrPz)_2]$ emerges as a compelling case study, given its coordination with the halogenated pyrazole ligand $C_3H_3N_2Br$, which may offer valuable insights into both its electronic properties and coordination environment under varying conditions.[19] Synthesized *via* a controlled Schlenk method approach, this compound exhibits an uncommon structural feature: the presence of two asymmetric halves per formula unit, suggesting new avenues for understanding metal–organic interactions and informing the design of stability-oriented materials.[20,21]

The structural and electronic properties of $[ZnCl_2(\eta^1\text{-}4BrPz)_2]$ were systematically investigated using a combined experimental and computational approach. Single-crystal X-ray diffraction (XRD) provided detailed structural elucidation, while infrared (IR) spectroscopy and Hirshfeld surface analysis offered further insights into bonding characteristics and intermolecular interactions. Additionally, Density Functional Theory (DFT) calculations, performed *via* the Vienna *Ab initio* Simulation Package (VASP), enabled precise predictions of the electronic band structure and density of states (DOS/PDOS).[22,23] Preliminary biological activity assessments also highlighted potential avenues for biocompatible applications.

The findings underscore the role of the brominated pyrazole ligand in enhancing both the electronic profile and structural stability of the compound, offering a performance advantage over conventional hybrid zinc halides. By addressing critical knowledge gaps in zinc coordination chemistry, this study advances the rational design of metal–organic halides for functional applications, especially where long-term stability and photophysical robustness are essential.

Beyond their structural and electronic importance, these compounds are increasingly explored for their biological potential. Rising antimicrobial resistance among common pathogens such as *Escherichia coli*, *Salmonella* spp., *Staphylococcus aureus*, and *Pseudomonas aeruginosa* has intensified the need for alternative antimicrobial agents,[24–27] as many conventional antibiotics are gradually losing effectiveness due to misuse and overuse.[27,28] Recent studies show that metal–organic systems, including zinc-, copper-, and cobalt-based halometallates, can display notable antibacterial activity[29–31] due to their tunable electronic structure and their ability to interact with microbial enzymes and cell membranes. These properties make zinc-based organic halides promising candidates for developing new antimicrobial materials, complementing their structural robustness and multifunctional behavior.

In summary, the unique coordination environment and asymmetric architecture of $[ZnCl_2(\eta^1\text{-}4BrPz)_2]$ position it as a promising candidate for optoelectronic devices, sensor platforms, and chemically resilient materials. These results contribute meaningfully to the expanding field of metal–organic halide chemistry and provide a foundation for the design of durable, tunable materials for advanced technological applications.

2 Experimental

2.1. Chemical materials

In this study, all reagents were of analytical grade and obtained from Sigma-Aldrich, including $ZnCl_2$ (99% purity), 4-bromopyrazole ($C_3H_3BrN_2$, 97%), and hydrochloric acid (HCl, 37%).

2.2. Synthesis of $[ZnCl_2(\eta^1\text{-}4BrPz)_2]$

4-Bromopyrazole and ethanol were used as received from commercial sources without further purification. The reaction was carried out under an inert nitrogen atmosphere using standard Schlenk techniques. Initially, 4-bromopyrazole (0.247 g, 1 mmol) was dissolved in 10 mL of absolute ethanol. This solution was then mixed with $ZnCl_2$ (0.136 g, 1 mmol) and 1 mL of 48% aqueous HCl in a glass flask and heated at 60 °C in an oil bath. Complete dissolution of the reagents was achieved after approximately 2 h.

The resulting solution was filtered and allowed to cool gradually in the oil bath, then left undisturbed at room temperature under ambient conditions to permit slow solvent evaporation. Colorless block-shaped crystals were obtained, isolated, and dried in a desiccator. Elemental analysis for $[ZnCl_2(\eta^1\text{-}4BrPz)_2]$ showed: C, 11.65 (calcd 11.52); H, 2.52 (2.31); N, 8.24 (8.12). IR data (KBr, cm^{-1}): ν(N–H$^+$) 1533; ν(C–N) 1647. The reaction afforded a yield of 0.422 g (98%). ESI-MS m/z: $[M-H]^-$ calculated 430.06, observed 430.24.

2.3. X-ray data collection

A single crystal with approximate dimensions of 0.27 × 0.17 × 0.09 mm^3 was selected for X-ray diffraction measurements at 100 K using an Xcalibur Atlas Gemini Ultra diffractometer with Mo-Kα radiation (λ = 0.71073 Å). Data processing was carried out using the SCALE3 ABSPACK program implemented in CrysAlisPro.[32] Data collection, reduction, and analysis were performed with SAINT,[33] and semi-empirical multi-scan absorption corrections were applied using SADABS.[34]

The structure was solved in the monoclinic space group $P2/c$ using automated procedures implemented in WINGX.[35] The molecular structure of $[ZnCl_2(\eta^1\text{-}4BrPz)_2]$ was determined by a dual-space approach with SHELXT-2018 [36] and subsequently refined by full-matrix least-squares methods using SHELXL-2019/3, (ref. 37) with anisotropic displacement parameters assigned to all non-hydrogen atoms. Inspection of the diffraction data indicated the presence of non-merohedral twinning. Accordingly, the structure was refined using a two-component twin model implemented in SHELXL. The twin law was defined by the matrix (−1 0 −1/0 −1 0/0 0 1) using the TWIN instruction. The refined BASF parameter converged to 0.412(1), indicating a significant contribution of the minor twin domain. All reflections from both components were included in the refinement, and appropriate scaling between the twin fractions was applied. The final refinement converged smoothly with satisfactory agreement indices and no significant residual electron density attributable to twinning, confirming the reliability of the structural model. All figures were prepared using

DIAMOND.[38] The refinement conditions and structural resolution of our compound are outlined in Table S1.

2.4. Spectroscopic measurement

Infrared (IR) and Raman measurements were performed in the 400–4000 and 0–3500 cm^{-1} ranges, respectively, using a PerkinElmer Spectrum 400 FTIR spectrometer equipped with a Universal Attenuated Total Reflectance (UATR) accessory and a Horiba LabRAM HR Evolution Raman spectrometer with a 532 nm excitation laser.

2.5. Thermal analysis

The thermal behavior of the $[ZnCl_2(\eta^1\text{-}4BrPz)_2]$ complex was examined by simultaneous thermogravimetric analysis (TGA) and differential scanning calorimetry (DSC) using a SETARAM TG–DSC 92 thermal analyzer. Measurements were carried out under a nitrogen atmosphere (flow rate: 100 mL min^{-1}) to ensure inert conditions. A sample mass of 2.687 mg was heated from 25 to 600 °C at a constant heating rate of 10 °C min^{-1}, allowing correlated mass-loss and thermal event analysis over the entire temperature range.

2.6. Hirshfeld surface analysis

To gain deeper insight into the intermolecular interactions previously observed within the crystal packing, we carried out a detailed analysis using Hirshfeld surfaces (HS).[39–44] The 3D Hirshfeld surfaces and the corresponding 2D fingerprint plots were generated with the Crystal Explorer 17.5 software.[45] The 3D Hirshfeld surface is defined by the normalized contact distance (d_{norm}), which is calculated based on three parameters: de (distance from a surface point to the nearest external nucleus), di (distance to the nearest internal nucleus), and the van der Waals radii of the atoms. The d_{norm} values were visualized on the Hirshfeld surface using a color gradient ranging from blue to red through white, providing a quantitative representation of intermolecular contacts.

2.7. Computational details

Periodic Density Functional Theory (DFT) calculations were performed using the Vienna *Ab Initio* Simulation Package (VASP), applying the projector-augmented wave (PAW) approach together with the Perdew–Burke–Ernzerhof (PBE) exchange–correlation functional. An energy cut-off of 600 eV was used for the plane-wave basis set. Sampling of the Brillouin zone was carried out using the KSPACING parameter fixed at 0.4,[46–53] which proved sufficient to yield stable optimized lattice parameters ($a = 21.7276$ Å, $b = 4.1482$ Å, $c = 13.8897$ Å) for the $[ZnCl_2(\eta^1\text{-}4BrPz)_2]$ system, in close agreement with experimental measurements ($a = 21.3691$ Å, $b = 4.0847$ Å, $c = 14.2396$ Å).

Electron Localization Function (ELF) distributions and structural representations were obtained using Vaspview and ChemCraft 1.6, respectively.[54,55] Non-covalent interaction (NCI) analyses were carried out with the CRITIC2 code,[56,57] and the corresponding NCI isosurfaces were visualized using VMD software.[58]

For docking studies and interaction analysis, homology models of the protein targets were constructed. The ligand geometry was optimized at the B3LYP/LANL2DZ level using Gaussian and then converted into PDB format for further use.[59] FASTA sequences of the receptors were obtained from the UNIPROTKB database and employed to identify appropriate templates for homology modeling through the SWISS-MODEL server hosted by EXPASY.[60] The generated models were subsequently analyzed to locate active sites using the ProFunc server and validated through Ramachandran plot evaluation.[61]

Molecular docking calculations were conducted using AutoDock Vina 1.5.7.[62,63] Prior to docking, crystallographic water molecules were removed, and polar hydrogens along with Kollman charges were added; all structures were then saved in PDBQT format. A grid box of 16 × 16 × 16 Å with *a* spacing of 1.0 Å was defined around the predicted binding regions to investigate antibacterial and antifungal activity. The receptor panel included DNA gyrase subunits A and B from nine bacterial species—four Gram-positive (*Staphylococcus aureus*, *Bacillus cereus*, *Enterococcus faecalis*, and *Micrococcus luteus*) and five Gram-negative (*Escherichia coli*, *Pseudomonas aeruginosa*, *Klebsiella pneumoniae*, *Salmonella enterica*, and *Salmonella typhi*)—as well as chitin synthase from two fungal species (*Aspergillus niger* and *Candida albicans*).[64] The grid box center coordinates are listed in Table S4. The binding pose associated with the lowest binding free energy (ΔG) was considered the most favorable (Table S4). Interaction diagrams and visual analyses were generated using Discovery Studio software (version 24.1.0.23298).[65]

In parallel with the docking study, pharmacokinetic properties were predicted *in silico* using the SwissADME web tool, allowing evaluation of key ADME parameters such as absorption, distribution, metabolism, excretion, drug-likeness, bioavailability, and potential cytochrome P450 interactions.

2.8. Methodology for determining antibacterial activity

The antibacterial properties of the zinc-based pyrazole halide $[ZnCl_2(\eta^1\text{-}4BrPz)_2]$ were investigated against eight pathogenic bacterial strains: *Enterococcus faecalis*, *Escherichia coli*, *Bacillus cereus*, *Pseudomonas aeruginosa*, *Staphylococcus aureus*, *Salmonella enterica*, *Salmonella typhi*, and *Micrococcus luteus*. Antibacterial activity was assessed using the agar well diffusion technique. Bacterial cultures were first grown overnight in nutrient broth at 37 °C and then standardized to the 0.5 McFarland turbidity ($\sim 1 \times 10^8$ CFU mL^{-1}). The resulting suspensions were uniformly inoculated onto sterile Mueller–Hinton agar plates, after which wells of 6 mm diameter were prepared and filled with different concentrations of the tested compound (0.5, 1, and 2 μg mL^{-1}). Tetracycline (1 μg mL^{-1}) served as the positive control, whereas sterile distilled water was used as the negative control.

Following incubation at 37 °C for 18–24 h, the inhibition zones surrounding each well were measured in millimeters using a digital caliper. All measurements were carried out in

triplicate, and the results were reported as mean values ± standard deviation. Antibacterial effectiveness was expressed in terms of inhibition zone diameter (mm), allowing comparison with the standard antibiotic.

The minimum inhibitory concentration (MIC) and minimum bactericidal concentration (MBC) were determined by the broth microdilution method. Bacterial suspensions were adjusted to 1×10^6 CFU mL^{-1} and exposed to a range of compound concentrations (0.2–5 μg mL^{-1}) in Mueller–Hinton broth, followed by incubation at 37 °C for 24 h. The MIC corresponded to the lowest concentration at which no visible bacterial growth was observed. For MBC determination, samples from clear wells were plated onto agar and incubated for an additional 24 h; the MBC was defined as the lowest concentration that resulted in no colony formation. All experiments were performed in triplicate.

2.9. Acute toxicity test

The acute toxicity of $[ZnCl_2(\eta^1\text{-}4BrPz)_2]$ and its free ligand was evaluated in male Wistar rats, aged two months and weighing 169 ± 8 g. Healthy animals were divided into groups of 5 rats and administered oral doses of 2, 4, 8, 16, and 32 mg per kg body weight for 14 days. During the treatment, animals were monitored for behavioral changes, weight loss, digestive disorders, or mortality. To assess hepatic and renal toxicity, biochemical parameters were measured: blood glucose (Biolabo kit n°87409), hepatic enzymes AST (Biolabo kit n°80025) and ALT (Biolabo kit n°80027), and renal markers creatinine (Biolabo kit n°90107) and urea (Biolabo kit n°80221), according to the manufacturer's instructions (Biolabo, Maizy, France).

3 Results and discussion

3.1. Description of the crystal structure

The newly synthesized $[ZnCl_2(\eta^1\text{-}4BrPz)_2]$ complex crystallizes in the centrosymmetric monoclinic space group $P2/c$, which features a two-fold rotation axis and an inversion center. The lattice parameters are as follows: $a = 21.3691(3)$ Å, $b = 4.0847(1)$ Å, $c = 14.2396(2)$ Å, with a β angle of 109.475(2)° and four formula units per unit cell ($Z = 4$). Interestingly, the asymmetric unit shown in Fig. 1 does not simply consist of one-half of the molecule, as might be expected given the inversion center located at the Zn cation (Zn^{2+}), which is coordinated with a chlorine atom and a 4-bromopyrazole molecule ($C_3H_3N_2Br$). Instead, the asymmetric unit contains two halves of two slightly different forms of the compound, leading to a Z' value of 1. This indicates that the asymmetric unit contains one complete molecule, which is divided into two halves reflecting subtle differences between the two forms. The small differences between these two forms are reflected in slight variations in bond lengths and angles, especially in the coordination geometry around the Zn center, and these minor discrepancies prevent the structure from being fully generated by symmetry from just one-half of a molecule. Despite the presence of an inversion center, the subtle differences between the two forms necessitate the inclusion of both halves in the asymmetric unit. These differences likely arise from local distortions or packing effects within the crystal lattice, which are common in coordination complexes where ligands can adopt slightly different conformations or orientations around the metal center. As a result, $Z' = 1$, meaning that the asymmetric unit contains enough information to describe one complete molecule, and the full unit cell, with $Z = 4$, contains four such complete molecules. This is in contrast to what would be expected if the molecule were perfectly symmetric, in which case the asymmetric unit could consist of only one half, yielding a Z' value of 0.5 and a corresponding $Z = 2$ for the unit cell.

The coordination environment around the Zn atom is particularly noteworthy. In both forms of the molecule shown in Fig. 2, Zn is coordinated by nitrogen and chloride ligands, forming a distorted tetrahedral geometry. However, the exact bond distances between Zn and its ligands differ slightly between the two forms, contributing to the non-equivalence of the two halves. The chloride ligands and all bonds in the organic molecules except the Br–C, C–H, and N–H, exhibit these slightly different bonding environments in each form, further distinguishing the two forms from one another. Additionally, the organic ligands coordinated to the Zn center may adopt slightly different orientations or conformations, which further contributes to the structural differences between the two forms.

From the provided bond-length data (Fig. 2), in the first distortion case, Zn_1 is coordinated to two nitrogen atoms (N_1 and N_1^I) with identical bond lengths of 2.021(3) Å, and two chloride atoms (Cl_1 and Cl_1^I), each with bond lengths of 2.2923(8) Å. The second distortion case involves Zn_2, where Zn_2–N_3 and Zn_2–N_3^{II} bonds measure 2.017(3) Å, while the Zn_2–Cl_2 and Zn_2–Cl_2^{II} bonds are slightly shorter than the first case at 2.2757(7) Å. These variations in bond lengths indicate local distortions around the Zn centers that arise due to slight packing differences and orientation of the ligands, contributing to the compound's subtle asymmetry. Despite the presence of an inversion center, these distortions result in a structure where the two Zn coordination polyhedra are not identical, increasing the overall complexity of the compound's crystallographic description. When considering the broader crystal structure as illustrated in Fig. 3, the projections along the b- and c-axes reveal a network of halogen–halogen interactions that further stabilize the packing within the unit cell.

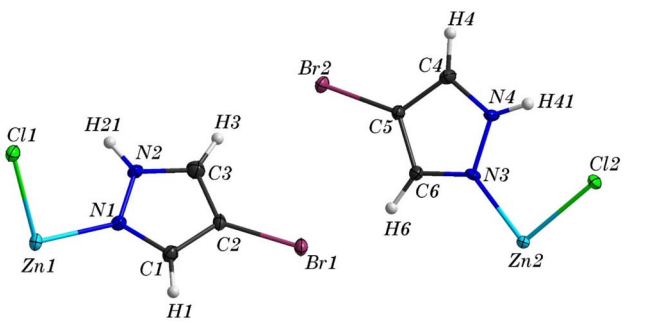

Fig. 1 Asymmetric unit of $[ZnCl_2(\eta^1\text{-}4BrPz)_2]$. Displacement ellipsoids are drawn at the 50% probability level.

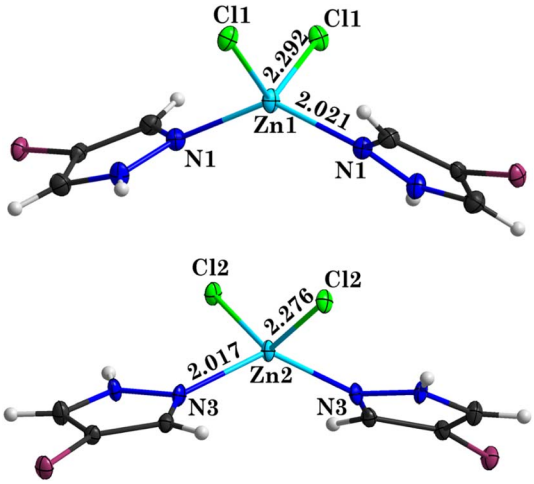

Fig. 2 The two crystallographically distinct Zn tetrahedra in the structure of $[ZnCl_2(\eta^1\text{-}4BrPz)_2]$.

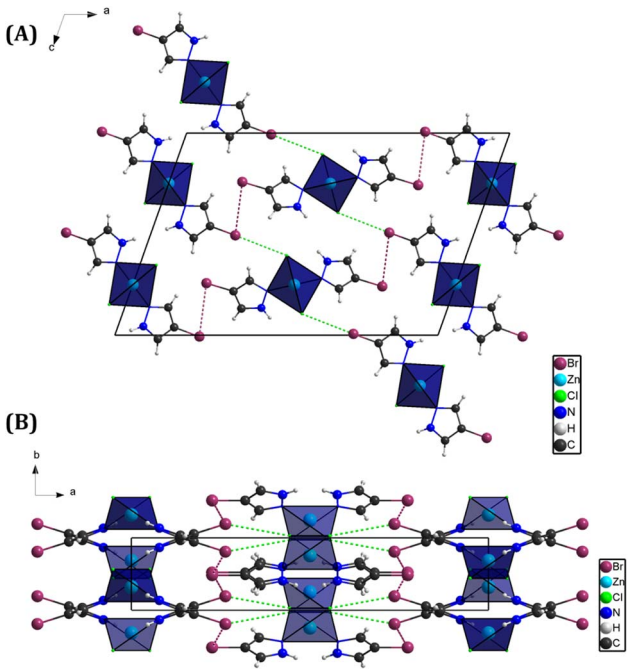

Fig. 3 Halogen–halogen interactions in the structure of $[ZnCl_2(\eta^1\text{-}4BrPz)_2]$ viewed along the *b*-axis (A) and the *c*-axis (B).

Two main types of halogen interactions can be observed: violet-colored Br···Br interactions with a distance of 3.823 Å, and green-colored Cl···Br interactions at 3.715 Å. These halogen–halogen contacts play a crucial role in reinforcing the crystal lattice, as they create a framework of non-covalent interactions that extend through the crystal. Such interactions are often seen in halogenated coordination compounds and contribute to the overall stability and arrangement of the molecules within the unit cell.

The projections clearly show how these halogen–halogen interactions form repeating motifs that connect adjacent

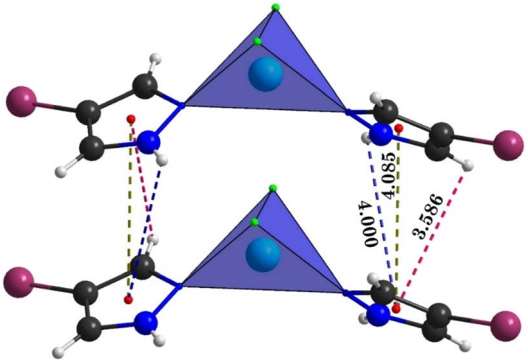

Fig. 4 Different types of π-interactions observed in the structure of $[ZnCl_2(\eta^1\text{-}4BrPz)_2]$: π···π (green), N–H···π (blue), and C–H···π (dark pink).

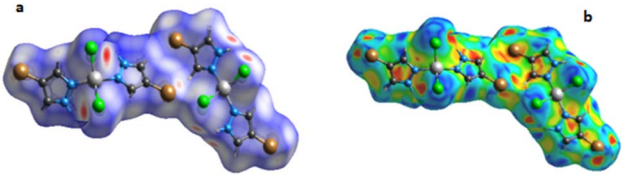

Fig. 5 3D Hirshfeld surfaces of $[ZnCl_2(\eta^1\text{-}4BrPz)_2]$ mapped over dnorm (a) and shape-index (b).

molecules, thereby influencing the spatial organization and contributing to the compound's stability. The close distances observed between the halogen atoms are consistent with known halogen bonding interactions, which are characterized by attractive forces between the halogen atoms and help in maintaining the structural integrity of the crystal lattice. In Fig. 4, the π-interactions are visualized, demonstrating another layer of structural stabilization in the compound. Several types of π-interactions are present, including π···π interactions (depicted in green), N–H···π interactions (blue), and C–H···π interactions (pink). These non-covalent interactions arise from the overlap of π-electron clouds between the aromatic systems of the organic ligands and contribute significantly to the crystal's cohesion. The π···π interactions occur between the aromatic rings of adjacent ligands, creating stacking arrangements that further stabilize the packing. The N–H···π and C–H···π interactions introduce additional hydrogen bonding-like contacts, further reinforcing the molecular assembly. Together, these π-interactions work synergistically with the halogen–halogen interactions (Cl···Br and Br···Br) to enhance the overall stability of the structure.

The combination of π and halogen bonding interactions creates a robust network of forces that counterbalances the slight distortions observed in the coordination environment around the Zn centers, allowing the compound to adopt a highly stable three-dimensional configuration. These intermolecular forces highlight the complex interplay between coordination geometry, π-stacking, and halogen bonding in defining the structural properties and stability of the compound.

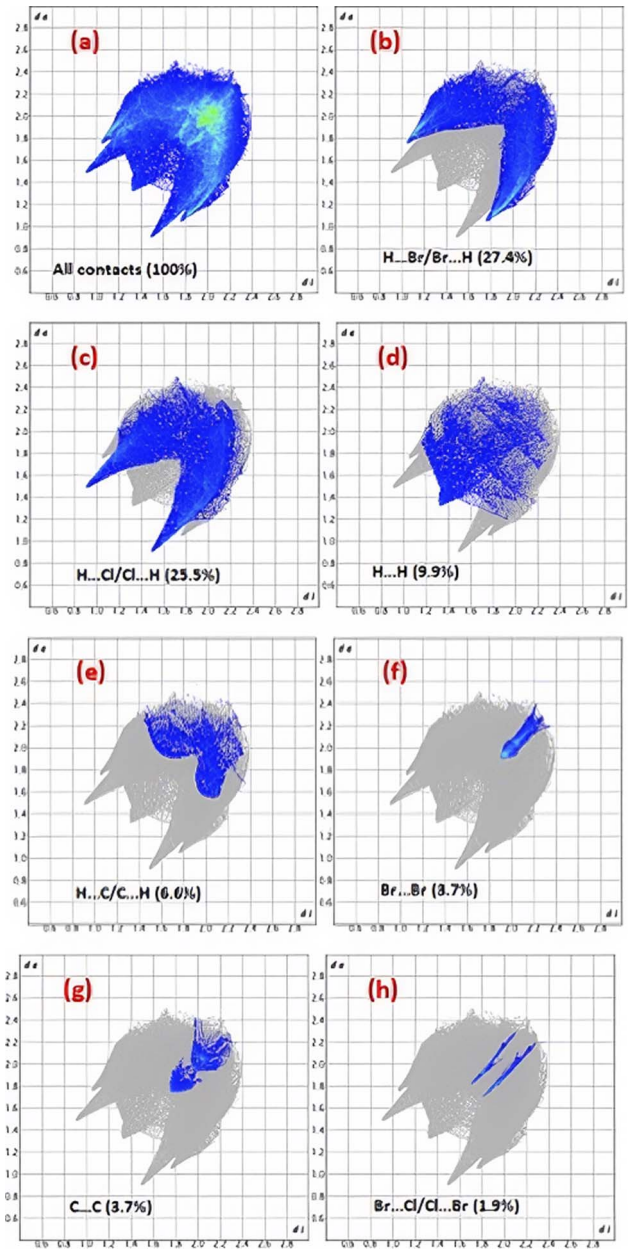

Fig. 6 Two-dimensional fingerprint plots of $[ZnCl_2(\eta^1\text{-}4BrPz)_2]$: (a) overall and decomposed into H···Br/Br···H (b), H···Cl/Cl···H (c), H···H (d), H···C/C···H (e), Br···Br (f), C···C (g), and Br···Cl/Cl···Br (h) interactions, with their percentage contributions to the Hirshfeld surface.

3.2. Hirshfeld surface analysis

The Hirshfeld surface analysis of the title compound is shown in Fig. 5, with mappings over *d*norm and the shape index. Prominent red regions on the *d*norm surface reveal the presence of short intermolecular contacts, mainly arising from H···Cl and H···Br interactions. Meanwhile, the shape index representation (Fig. 5) exhibits alternating red and blue triangular patterns that reflect concave and convex surface regions, providing evidence of π–π stacking between adjacent molecules.

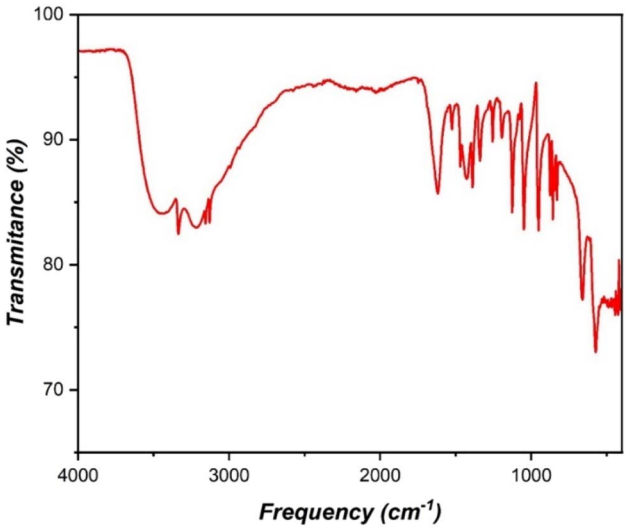

Fig. 7 Infrared spectrum of $[ZnCl_2(\eta^1\text{-}4BrPz)_2]$.

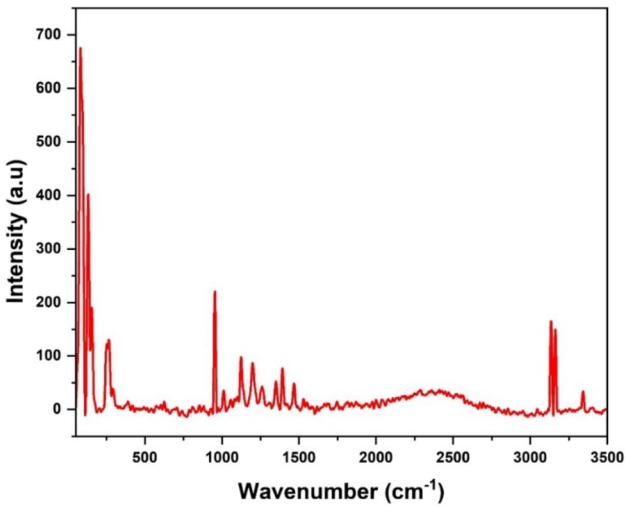

Fig. 8 Raman spectrum of $[ZnCl_2(\eta^1\text{-}4BrPz)_2]$.

The 2D fingerprint plots can be deconstructed to highlight specific atom pair contacts, enabling the differentiation of interaction types that overlap within the complete fingerprint profile (Fig. 6a).

The initial findings of this study corroborate the structural analysis, confirming the weak C–H···Cl and N–H···Cl hydrogen bonding interactions and emphasizing the predominance of van der Waals interactions, notably H···Br/Br···H contacts (27.4%), which play a crucial role in stabilizing the title compound (Fig. 6b). Furthermore, Fig. 6c indicates that H···Cl/Cl···H interactions, comprising 25.5%, make a significant contribution to crystal stability through noncovalent interactions. The study also recognizes the presence of other, less dominant interactions, such as H···H, H···C/C···H, and C···C, as well as Br···Br, with contributions of 9.9%, 6.6%, and 3.7%, respectively. Of particular note is the halogen–halogen

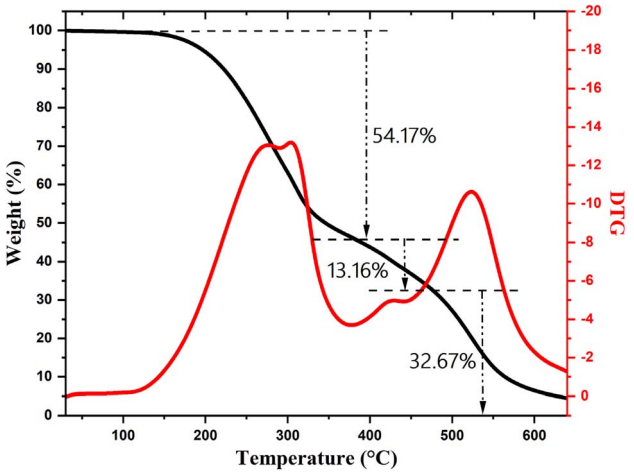

Fig. 9 Decomposition analysis of $[ZnCl_2(\eta^1\text{-}4BrPz)_2]$ *via* simultaneous TGA and DTG.

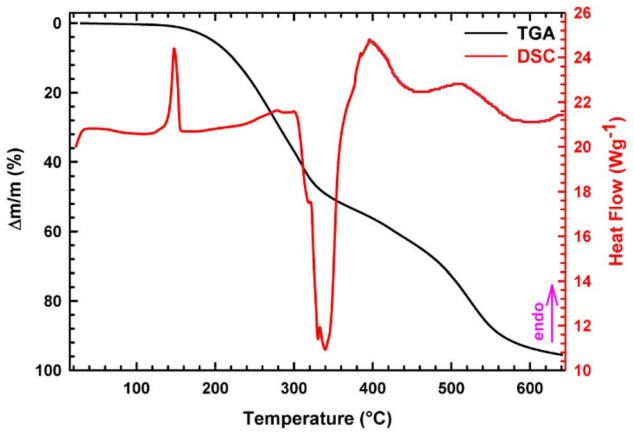

Fig. 10 Simultaneous TGA-DSC curves for the decomposition of $[ZnCl_2(\eta^1\text{-}4BrPz)_2]$.

interaction, Br···Cl/Cl···Br, which, despite its lower contribution of 1.9%, plays a critical role in reinforcing the structural cohesion.

3.3. Vibrational studies

The vibrational analysis of $[ZnCl_2(\eta^1\text{-}4BrPz)_2]$, combining IR (Fig. 7) and Raman (Fig. 8) spectroscopy, reveals comprehensive insights into the compound's structural and bonding characteristics. The study effectively identifies and correlates vibrational modes across both spectroscopic techniques, enabling a nuanced understanding of the molecule's coordination environment, metal–ligand interactions, and ligand dynamics.[69,70] The high-energy vibrational bands observed in both IR (3336 cm^{-1}) and Raman (3342 cm^{-1}) are attributed to symmetric N–H stretching vibrations, characteristic of aromatic nitrogen donors. Complementary Raman peaks at 3161 and 3135 cm^{-1}, along with the IR peak at 3129 cm^{-1}, highlight the asymmetric stretching of aromatic C–H bonds, showcasing the involvement of sp^2 hybridized carbon in the heterocyclic ligand framework. These modes confirm the robust aromaticity and the minimal distortion of the ligand upon coordination to Zn. In the mid-frequency range, distinct C=N and C=C stretching vibrations are evident in IR (1618 and 1523 cm^{-1}, respectively) and Raman (1466 cm^{-1}), signifying strong delocalization within the ligand backbone. These observations align with the coordination-induced stabilization of electronic density in the heterocyclic system. C–N stretching (1388 cm^{-1}) and C–H bending vibrations (1427 cm^{-1}) further emphasize the ligand's contribution to the overall coordination environment. Low-frequency modes provide critical insights into metal–ligand interactions. Both IR and Raman spectra exhibit a significant peak at 1125 cm^{-1}, corresponding to Zn–N stretching, which underscores the primary coordination role of the nitrogen donor atoms. Zn–Cl stretching vibrations are prominently detected in IR at 1048 cm^{-1} and Raman modes at lower frequencies (856–829 cm^{-1}). C–Br interactions are identified at 660 cm^{-1} in the IR spectrum, reflecting the diversity of halide coordination in the complex.

Raman spectroscopy also uncovers unique torsional and bending modes not visible in IR, particularly at 258, 155, 131, and 81 cm^{-1}. These low-energy modes highlight the dynamic behavior of the coordination framework and potential ligand–metal coupling. Framework bending and deformation, detected at 573 and 424 cm^{-1} in the IR spectrum, further emphasize the

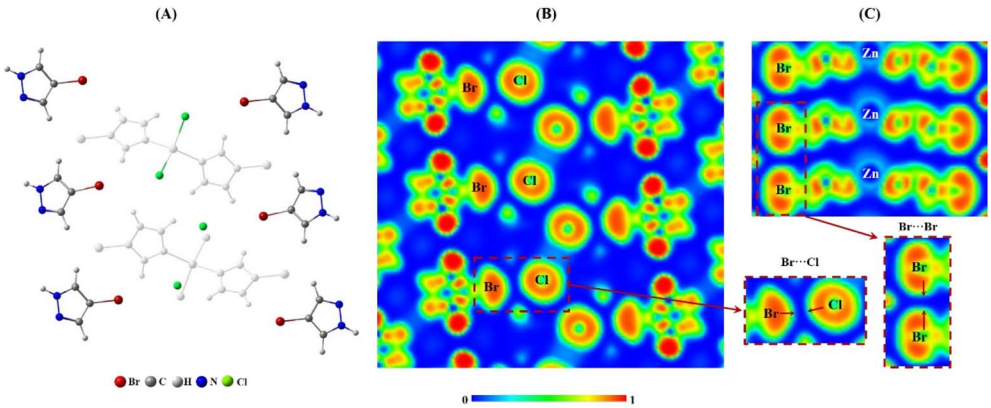

Fig. 11 Geometry represented in 2D (A) and ELF contour plots for $[ZnCl_2(\eta^1\text{-}4BrPz)_2]$ (B and C).

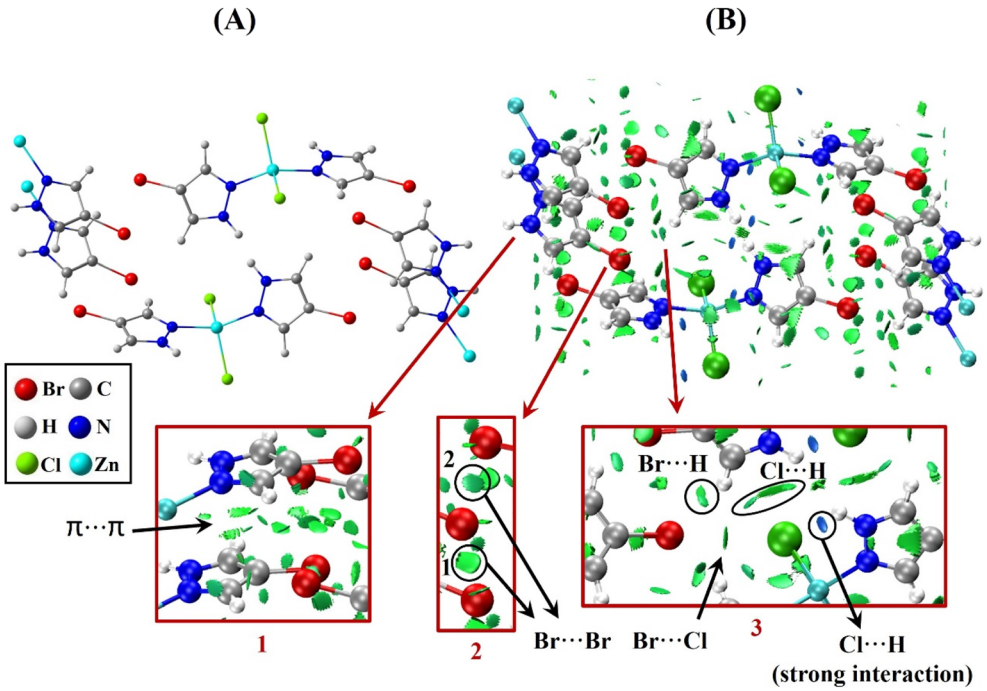

Fig. 12 NCI plots for $[ZnCl_2(\eta^1\text{-}4BrPz)_2]$ (B) for the geometry represented in 2D (A).

flexibility and subtle asymmetry in the crystal lattice, consistent with variations in bond lengths between the two halves of the asymmetric unit.

3.4. Thermal studies

The thermal behavior of the compound $[ZnCl_2(\eta^1\text{-}4BrPz)_2]$ was thoroughly examined using simultaneous thermogravimetric analysis (TGA) and differential scanning calorimetry (DSC), yielding critical insights into its decomposition pathway and thermal stability. The TGA curve delineates three distinct decomposition steps, each well-correlated with corresponding peaks in the derivative thermogravimetric (DTG) data. The first stage, spanning from 120 °C to 300 °C, demonstrates a combined weight loss of 54.17%, attributed to the overlapping decomposition of Br_2 (theoretical: 37.14%) and the subsequent degradation of the organic moiety, 6C, in the form of CO_2 (theoretical: 17.66%).[66] The theoretical calculation for this combined step yields a total weight loss of 54.8%, showing exceptional agreement with the experimental value and reflecting a minimal error percentage of approximately 0.63%. This overlap is evident in the broad DTG peak covering the respective temperature range, where the initial release of Br_2 transitions seamlessly into the degradation of the aromatic organic fragment. The second decomposition stage, identified

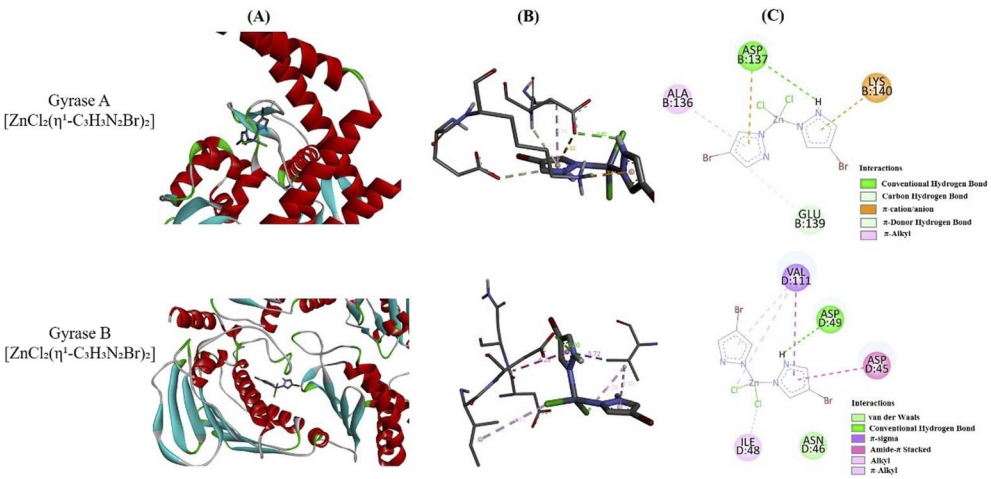

Fig. 13 Interaction analysis of the docking between $[ZnCl_2(\eta^1\text{-}4BrPz)_2]$ and *Escherichia coli*. (A) Representation of the binding pocket. (B) Most stable receptor–ligand complex shown in 3D, including bond distances (Å), along with the corresponding 2D interaction diagram (C).

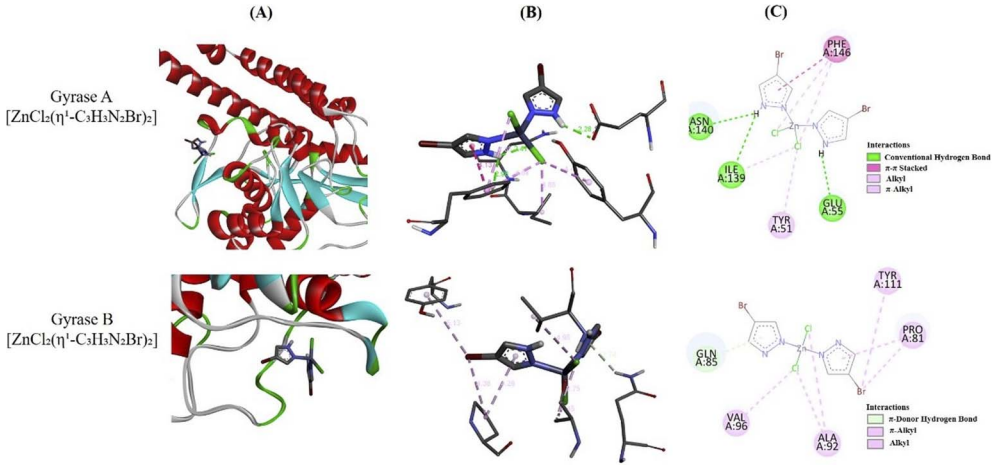

Fig. 14 Interaction profile of the docking between $[ZnCl_2(\eta^1\text{-}4BrPz)_2]$ and *Enterococcus faecalis*. (A) Visualization of the binding pocket. (B) Most stable receptor–ligand configuration displayed in 3D, including bond distances (Å), together with the corresponding 2D interaction scheme (C).

as a weight loss of 13.16%, corresponds to the breakdown of the N_4H_2 fragment. The theoretical weight loss for this event is calculated to be 13.50%, resulting in an error margin of just 2.52%, which underscores the accuracy of this attribution. The final stage of decomposition, responsible for a weight loss of 32.67%, is linked to the formation of $ZnCl_2$ residue. This experimental value aligns closely with the theoretical weight loss of 31.70%, showing an error percentage of 2.98%. The overall consistency between the theoretical and experimental weight losses, as reflected in these small error percentages, validates the reliability and precision of the proposed decomposition pathway.

Complementary DSC data provides additional insights into the thermal events occurring within the compound. The first endothermic peak, detected in the range of 133 °C to 157 °C with a peak at approximately 148 °C, initially suggested either the fusion of the compound or a structural phase transition. Notably, this temperature range exhibited no corresponding weight loss in the TGA data, ruling out decomposition as a possibility. The absence of thermal decomposition strongly indicated that this event was non-destructive, consistent with a physical transformation. While distinguishing between the two possibilities (fusion or structural phase transition) was initially challenging, subsequent analysis revealed that the fusion temperature of the compound, determined in separate analysis, was different from 148 °C, thereby eliminating fusion as a plausible explanation. The identification of this phase transition highlights the compound's dynamic structural properties under thermal stress.

The second significant DSC peak, an exothermic event between 300 °C and 377 °C, is directly associated with the decomposition processes observed in the TGA. This peak corresponds to the breakdown of the organic ligand and halogen components, affirming the sequential thermal events

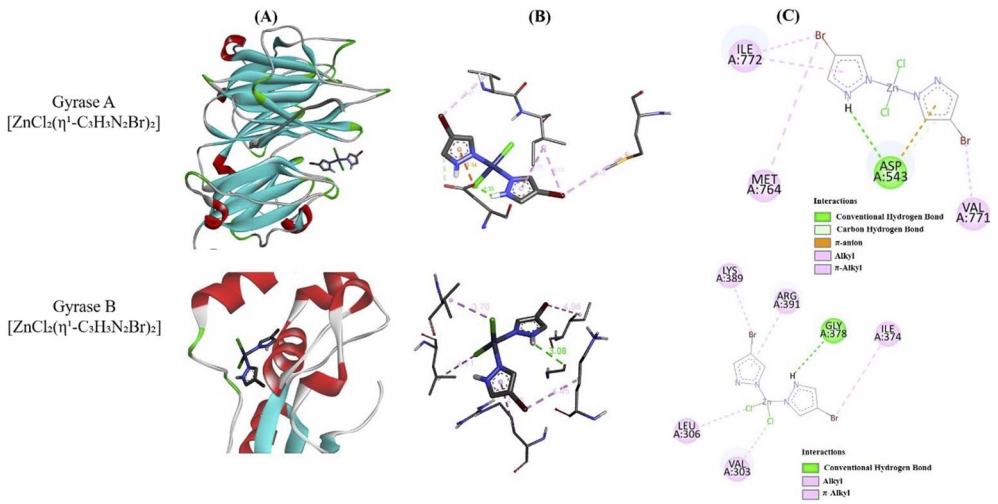

Fig. 15 Interaction analysis of the docking between $[ZnCl_2(\eta^1\text{-}4BrPz)_2]$ and *Bacillus cereus*. (A) Depiction of the binding pocket. (B) Lowest-energy receptor–ligand arrangement shown in 3D, including bond distances (Å), along with the corresponding 2D interaction representation (C).

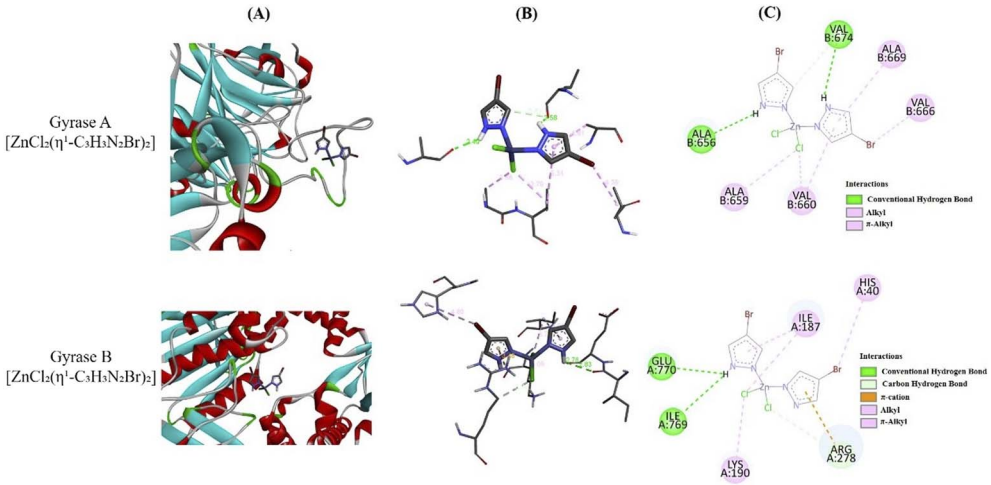

Fig. 16 Interaction analysis of the docking between $[ZnCl_2(\eta^1\text{-}4BrPz)_2]$ and *Pseudomonas aeruginosa*. (A) Illustration of the binding pocket. (B) Most energetically favorable receptor–ligand configuration shown in 3D with bond distances (Å), accompanied by the corresponding 2D interaction diagram (C).

outlined by the TGA. Collectively, the TGA and DSC results provide a detailed understanding of the thermal stability, phase behavior, and decomposition pathway of $[ZnCl_2(\eta^1\text{-}4BrPz)_2]$, underscoring the compound's structural integrity at elevated temperatures and its decomposition into well-defined components. The precise correlation between experimental data and theoretical predictions further demonstrates the robustness and accuracy of the thermal analysis methodology employed. The thermogravimetric analysis (TGA) and differential scanning calorimetry (DSC) curves of the complex $[ZnCl_2(\eta^1\text{-}4BrPz)_2]$ are illustrated in Fig. 9 and 10, respectively.

3.5. ELF and NCI analysis

ELF and NCI analyses were conducted for the $[ZnCl_2(\eta^1\text{-}4BrPz)_2]$ system in order to better understand its structural stability from an electronic perspective. The ELF distribution corresponding to the plane defined by Br and Cl atoms is presented in Fig. 11B, based on the geometry shown in Fig. 11A. For clarity, atoms located below this plane are omitted (displayed in white). The ELF visualization is primarily centered on the bromine atoms (Fig. 11B and C).

A closer inspection of the enlarged region in Fig. 11B reveals that the ELF contours associated with Br atoms are oriented toward those of Cl atoms, and *vice versa*. This directional localization of electron density suggests the presence of Br···Cl interactions that contribute to the overall stability of the structure. Fig. 11C illustrates another ELF section of the compound, focusing on the Br atom bonded to the pyrazole ring. In the magnified area, the electron density around the Br atoms (green regions) is clearly directed toward neighboring Br atoms positioned above or below, as highlighted by the red arrows.

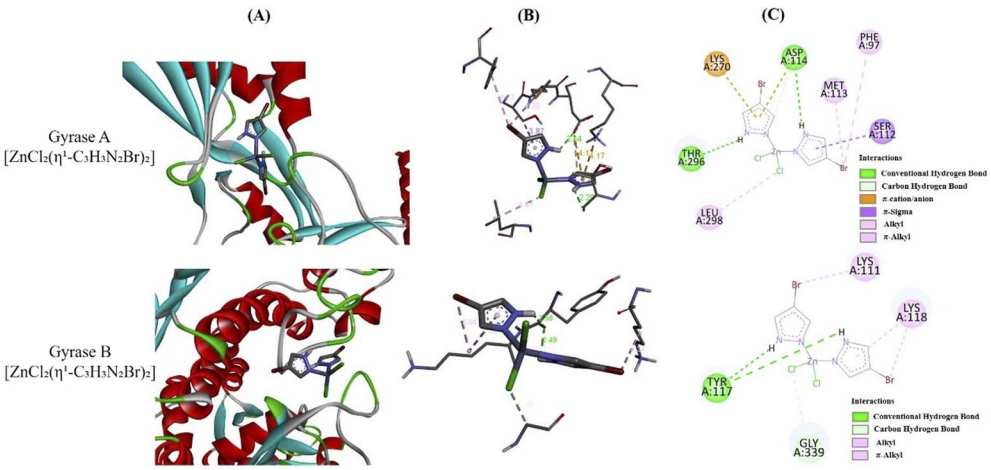

Fig. 17 Interaction analysis of the docking between $[ZnCl_2(\eta^1\text{-}4BrPz)_2]$ and *Staphylococcus aureus*. (A) Representation of the binding site. (B) Most stable receptor–ligand conformation visualized in 3D, including bond distances (Å), along with the corresponding 2D interaction diagram (C).

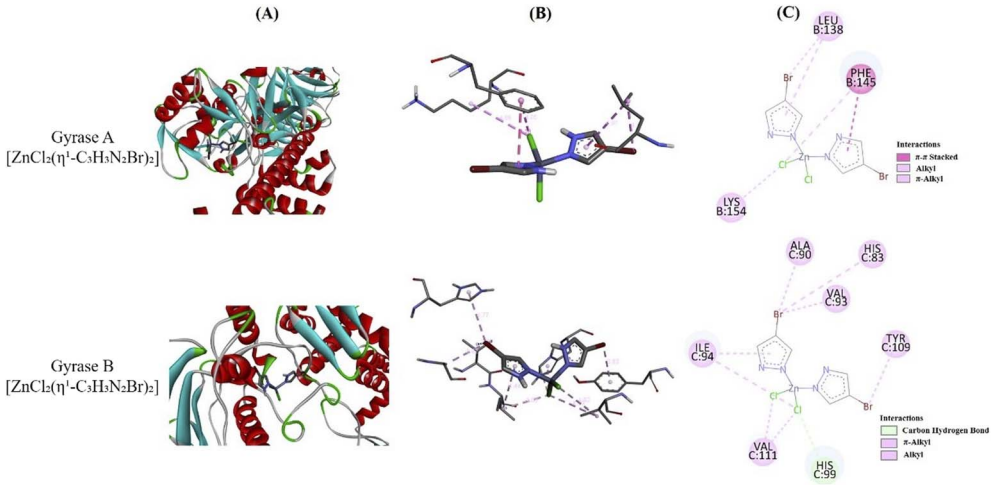

Fig. 18 Interaction analysis of the docking between $[ZnCl_2(\eta^1\text{-}4BrPz)_2]$ and *Salmonella enterica*. (A) Visualization of the binding site. (B) Lowest-energy receptor–ligand complex presented in 3D with bond distances (Å), together with the corresponding 2D interaction diagram (C).

Such features provide evidence for Br···Br interactions, which play an important role in maintaining the cohesion of the crystal lattice. In addition, the green regions observed in the ELF map around the pyrazole ring (Fig. 11C) indicate the presence of π···π stacking interactions, further contributing to structural stabilization. These non-covalent interactions—including halogen···halogen contacts, π···π stacking, and hydrogen bonding—are also supported by the NCI analysis.

The NCI approach relies on color-coded isosurfaces to qualitatively describe weak intermolecular interactions: blue regions correspond to strong attractive interactions, green regions indicate weak stabilizing contacts, and red regions represent repulsive interactions.

Fig. 12 shows the NCI plots for the $[ZnCl_2(\eta^1\text{-}4BrPz)_2]$ structure focus the analysis on the geometry represented in 2D in Fig. 12A. The NCI analysis in Fig. 12B shows green stabilizing isosurfaces. In the red enhanced rectangles it is shown the isosurfaces for clarity of explanation purposes. Thus the green isosurfaces observed between pyrazole rings indicates stabilizing π···π stacking interactions.

In the second red rectangle of Fig. 12B it is shown two Br···Br interactions indicated in the black circles. The first circle represent the Br···Br stabilizing interaction corresponding to the Br atoms between the stacking pyrazole rings. But, the second black circle represents the Br···Br interactions between units of $[ZnCl_2(\eta^1\text{-}4BrPz)_2]$. This interaction play an important role in stabilizing the structure because it is of greenish blue colour that implies a stronger interaction than those of green colour (weak stabilizing interaction). In the third red rectangle two types of interactions are detected. First corresponds to stabilizing Br···Cl interactions. The second interaction are of hydrogen bond type. It is observed green lobes between Br, Cl and H atoms that stabilizes the system. But it is remarkable the blue lobes observed for the interaction between the Cl and H

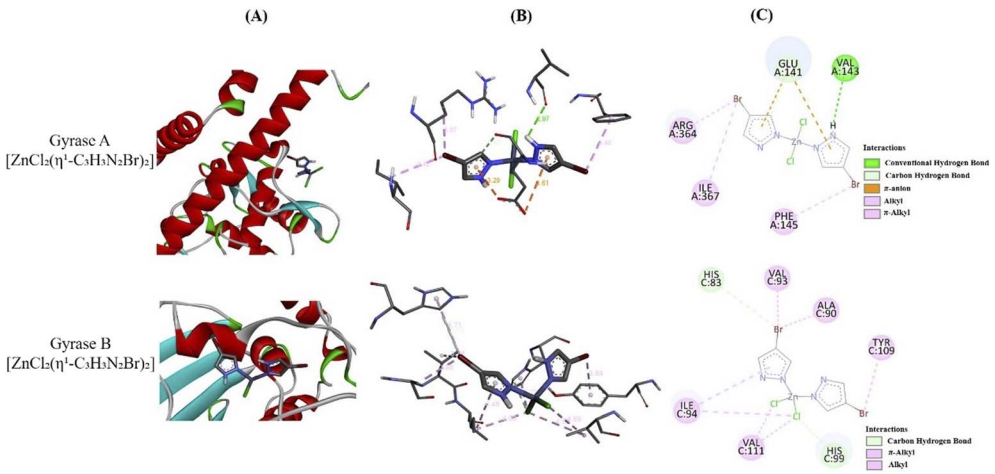

Fig. 19 Interaction analysis of the docking between $[ZnCl_2(\eta^1\text{-}4BrPz)_2]$ and *Salmonella typhi*. (A) Depiction of the binding pocket. (B) Most favorable receptor–ligand conformation illustrated in 3D with bond distances (Å), along with the corresponding 2D interaction scheme (C).

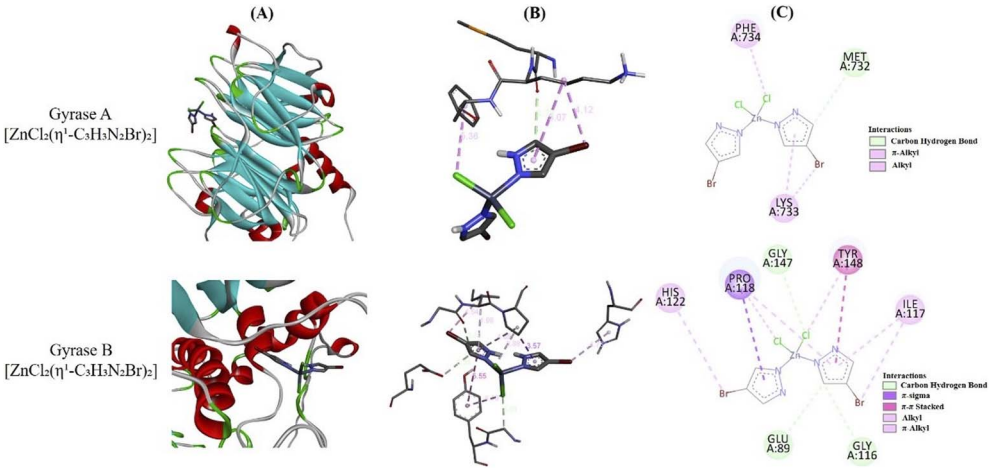

Fig. 20 Interaction analysis of the docking between $[ZnCl_2(\eta^1\text{-}4BrPz)_2]$ and *Micrococcus luteus*. (A) Illustration of the binding site. (B) Most stable receptor–ligand configuration shown in 3D with bond distances (Å), accompanied by the corresponding 2D interaction diagram (C).

atom from the pyrazole ring of each unit that clearly indicates an strong stabilizing interaction that helps to stabilize each $[ZnCl_2(\eta^1\text{-}4BrPz)_2]$ unit. Therefore, both ELF and NCI results reveal the inner characteristics of the structure to interact through the Cl, Br atoms and the capacity to form hydrogen bonds when acting as ligand with other compounds as proteins, as it will be shown later in the docking analysis.

3.6. *In silico* evaluation of the antimicrobial activities of $[ZnCl_2(\eta^1\text{-}4BrPz)_2]$

The antibacterial and antifungal potential of $[ZnCl_2(\eta^1\text{-}4BrPz)_2]$ against Gram-positive and Gram-negative bacteria, as well as fungi, was investigated through molecular docking studies (Table S4). To support these findings, an *in silico* ADME analysis was also carried out to assess the compound's pharmacokinetic properties. DNA gyrase (subunits A and B) was selected as the bacterial target due to its essential role in DNA replication, while chitin synthase was chosen for fungi because of its involvement in chitin biosynthesis and transport, which are critical for maintaining the fungal cell wall.

Table S4 summarizes the results for nine bacterial strains—four Gram-positive (*Staphylococcus aureus*, *Bacillus cereus*, *Enterococcus faecalis*, and *Micrococcus luteus*) and five Gram-negative (*Escherichia coli*, *Pseudomonas aeruginosa*, *Klebsiella pneumoniae*, *Salmonella enterica*, and *Salmonella typhi*)—along with two fungal species (*Aspergillus niger* and *Candida albicans*). The most stable binding mode for each system was identified based on the lowest binding free energy (ΔG). Since hydrogen bonding plays a key role in protein–ligand stability, Table S4 also reports the nature of these interactions, including the residues involved and the corresponding distances. The identified hydrogen bonds include conventional, carbon–hydrogen, and π-donor types. Conventional hydrogen bonds involve

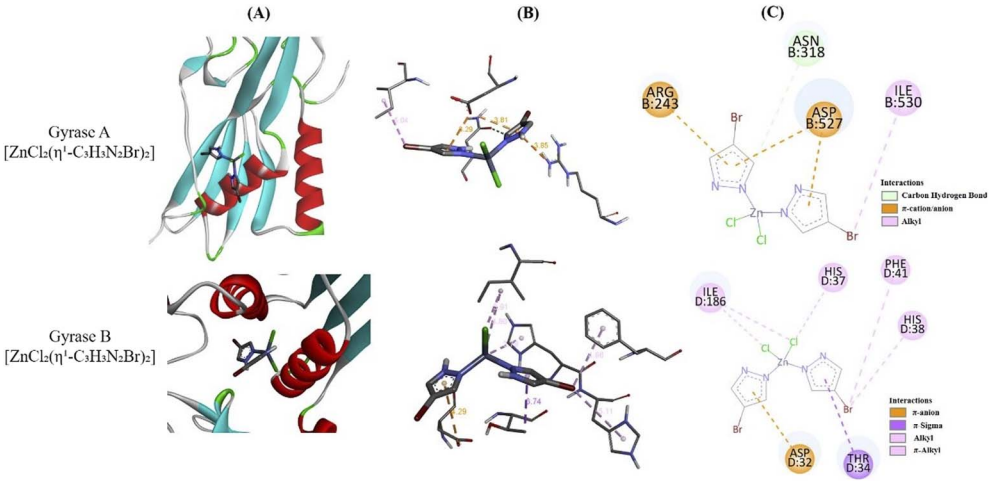

Fig. 21 Interaction analysis of the docking between $[ZnCl_2(\eta^1\text{-}4BrPz)_2]$ and *Klebsiella pneumoniae*. (A) Representation of the binding pocket. (B) Most energetically favorable receptor–ligand complex displayed in 3D with bond distances (Å), together with the corresponding 2D interaction diagram (C).

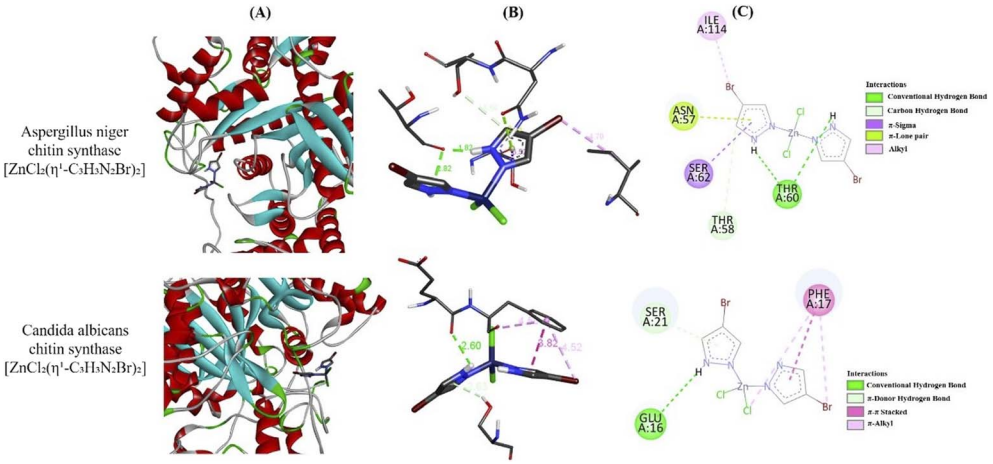

Fig. 22 Interaction profile for the docking between $[ZnCl_2(\eta^1\text{-}4BrPz)_2]$ and chitin synthase of both Aspergillus Niger and Candida albicans. (A) Binding site. (B) More favourable conformation between the receptor and ligand in 3D with bond distances (Å) and its 2D diagram (C).

hydrogen atoms bound to electronegative atoms such as N, O, P, or S. In contrast, carbon–hydrogen bonds arise when a polarized carbon atom acts as the donor, leading to weaker interactions. π-Donor hydrogen bonds occur when a π-system functions as an acceptor interacting with a hydrogen donor.

The energetic data (Table S4) indicate that binding to Gyrase B is generally more favorable than to Gyrase A, with the exception of *Klebsiella pneumoniae*, where the Gyrase A complex is slightly more stable by 0.4 kcal mol^{-1}. Overall, binding energies fall within the range of approximately −4 to −5 kcal mol^{-1}, suggesting comparable antibacterial and antifungal activity across the studied organisms. The most favorable interaction was observed for Gyrase B of *Escherichia coli* (−5.3 kcal mol^{-1}), followed by *Enterococcus faecalis*, *Bacillus cereus*, *Pseudomonas aeruginosa*, *Staphylococcus aureus*, *Salmonella enterica*, *Salmonella typhi*, *Micrococcus luteus*, and *Klebsiella pneumoniae*. In the case of fungi, the strongest binding was found for chitin synthase from *Aspergillus niger* (−4.7 kcal mol^{-1}), followed by *Candida albicans* (−4.1 kcal mol^{-1}).[67]

A more detailed analysis of bacterial systems is presented according to the energetic ranking for Gyrase B. For *Escherichia coli* (−5.3 kcal mol^{-1}), hydrogen bonding is observed between the ASP49 residue (3.00 Å) and the pyrrolic hydrogen of the pyrazole moiety (Fig. 13). Additional interactions include van der Waals contacts with ASN46, as well as π–sigma, π–alkyl, and alkyl interactions involving VAL111 and ILE48, and π–π stacking with ASP45. In contrast, docking with Gyrase A (−3.1 kcal mol^{-1}) shows hydrogen bonding with ASP137 (2.62

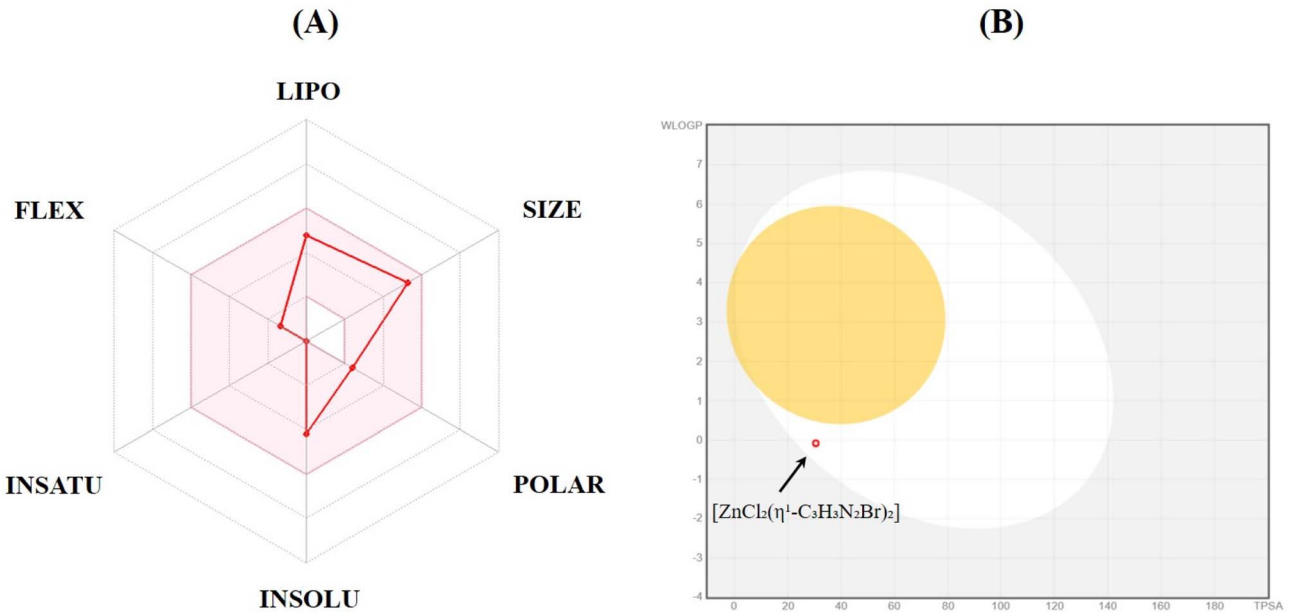

Fig. 23 Bioavailability (A) and ADME Boiled-Egg model (B) for $[ZnCl_2(\eta^1\text{-}4BrPz)_2]$.

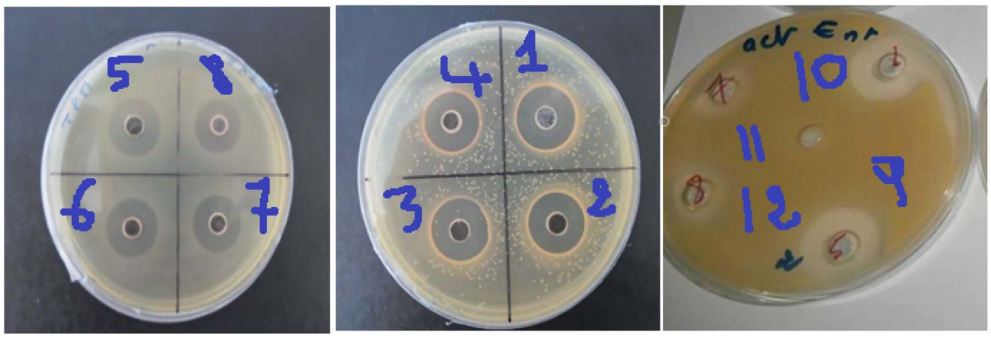

Fig. 24 Antibacterial activity of tetracycline (1 μg mL^{-1}) against 11 microbial strains. The zones of inhibition (in mm) are shown for each microorganism: (1) tetracycline, (2) *Enterococcus faecalis*, (3) *Escherichia coli*, (4) *Bacillus cereus*, (5) *Pseudomonas aeruginosa*, (6) *Staphylococcus aureus*, (7) *Salmonella enterica*, (8) *Salmonella typhi*, (9) *Micrococcus luteus*, (10) *Klebsiella pneumoniae*, (11) *Aspergillus niger*, and (12) *Candida albicans*.

Å), a carbon–hydrogen interaction with GLU139 (3.53 Å), and π-based interactions with ALA136 and LYS140 (Fig. 3).

The interaction between $[ZnCl_2(\eta^1\text{-}4BrPz)_2]$ and Gyrase B from *Enterococcus faecalis* has a energy of −4.9 kcal mol^{-1} (Table S6). For this docking it is observed π-donor hydrogen bond (2.74 Å) between the GLN85 and the pyrazole ring also π-alkyl interaction with PRO81 and alkyl interactions with ALA92, VAL96 and TYR111 (Fig. 14). For the interaction with Gyrase A (−3.9 kcal mol^{-1}) the docking shows the presence of conventional hydrogen bonds with GLU55 (2.28 Å), ILE139 (2.98 Å) and ASN140 (2.41 Å), alkyl and π-alkyl with TYR51, and π–π stacked with PHE146 (Fig. 14).

Fig. 15 shows the docking between $[ZnCl_2(\eta^1\text{-}4BrPz)_2]$ and Bacillus cereus. For the docking with Gyrase B of Bacillus cereus (−4.7 kcal mol^{-1}) it is observed conventional hydrogen bond with GLY378 (3.08 Å), alkyl interactions with VAL303, LEU306, ILE374, LYS389 and π-alkyl interactions with ARG391. The interaction with Gyrase A (−4.1 kcal mol^{-1}), shows hydrogen bond interaction with ASP543 (2.35 Å) as well as alkyl and π–alkyl interactions with MET764, VAL771 and ILE772, respectively.

For the docking with *Pseudomonas aeruginosa* Gyrase B (−4.6 kcal mol^{-1}) is observed three hydrogen bonds interactions with ILE769 (2.76 Å), GLU770 (2.83 Å) and ARG278 (3.70 Å), π–alkyl interaction with ILE187, and alkyl interactions of HIS40, ILE187 and LYS190 with halogenated atoms of $[ZnCl_2(\eta^1\text{-}4BrPz)_2]$ (Fig. 16). For the interaction with Gyrase B (−4.6 kcal mol^{-1}) are detected two hydrogen bonds between ALA656 (2.40 Å) and VAL674 (2.58 Å) with the pirrolic hydrogens of each pirazole ring, two π–alkyl interactions with VAL660 and ALA669, and alkyl interactions of ALA659, VAL660 and VAL666 with the halogen atoms (Fig. 16).

Fig. 17 shows the docking between $[ZnCl_2(\eta^1\text{-}4BrPz)_2]$ and *Staphylococcus aureus* Gyrase. The interaction profile for the docking between $[ZnCl_2(\eta^1\text{-}4BrPz)_2]$ and *Staphylococcus aureus* Gyrase B (−4.5 kcal mol^{-1}) shows conventional hydrogen bond between both pirrolic hydrogens of the complex and oxygen atoms of TYR117 (2.58 and 2.49 Å), a carbon hydrogen bond with GLY339 (3.40 Å), π–alkyl with LYS118, and alkyl interactions of LYS 111 and LYS118 with both Br atoms. The docking with Gyrase A (−4.3 kcal mol^{-1}) shows conventional hydrogen bonds with ASP114 (2.44 Å) and THR296 (2.29 Å), π–sigma and π–alkyl with SER112, LYS270, alkyl interactions with PHE97, MET113 and LEU298 (Fig. 17).

The docking of *Salmonella enterica* Gyrase B (−4.5 kcal mol^{-1}) shows carbon hydrogen bond with HIS99 (3.22Å), π–alkyl with ILE94, and alkyl interactions of HIS83, ALA90, VAL93, ILE94, TYR109 and VAL111 with halogen atoms (Fig. 18). For the docking with Gyrase A (−4.2 kcal mol^{-1}). It is observed π–π stacked and π–alkyl interactions with PHE145 and LEU138, respectively, as well as alkyl interactions with LEU138 and LYS154 (Fig. 18).

In case of the docking of *Salmonella typhi* Gyrase B (−4.5 kcal mol^{-1}) it is observed carbon hydrogen bonds of HIS83 (3.77 Å) and HIS99 (3.24 Å) with Br and Cl atoms of $[ZnCl_2(\eta^1\text{-}4BrPz)_2]$, respectively. It is also detected alkyl interactions with VAL93, ALA90, ILE 94, TYR109 and π–alkyl interactions with ILE94 (Fig. 19). For Gyrase A (−4.1 kcal mol^{-1}) it is detected a conventional hydrogen bond of VAL143 (2.97 Å) with pirrolic hydrogen from pirazole ring, and a carbon hydrogen bond with GLU141 (3.46 Å). Alkyl interactions are shown between PHE145, ARG364 and ILE367 and Br atoms of the complex (Fig. 19).

Fig. 20 shows the interaction profile for the docking between $[ZnCl_2(\eta^1\text{-}4BrPz)_2]$ and Micrococcus luteus. The docking analysis for the interaction between $[ZnCl_2(\eta^1\text{-}4BrPz)_2]$ and Micrococcus luteus Gyrase B (−4.4 kcal mol^{-1}) shows carbon hydrogen bonds with GLU89 (3.26 Å), GLY147 (3.01 Å) and GLY116 (3.66 Å), π-sigma with PRO118, π–alkyl with ILE117, π–π shaped with TYR148, alkyl interactions with HIS122 and ILE117 (Fig. 20). For the interaction with Gyrase A (−3.6 kcal mol^{-1}) a carbon hydrogen bond is detected with MET732 (3.79 Å), π–alkyl with LYS733, and alkyl interactions with both LYS733 and PHE734 (Fig. 20).

The docking with Gyrase B of *Klebsiella pneumoniae* (−3.7 kcal mol^{-1}) shows π interactions with THR34 and ASP32, π-alkyl with HIS37, HIS38 and PHE41 and alkyl interactions between ILE186 and Cl atoms of the Zn complex (Fig. 21). In case of Gyrase A (−4.1 kcal mol^{-1}), carbon hydrogen bonds are found with ASN318 (3.70 Å) that stabilizes the system, π

interactions with ARG243 and ASP527, and alkyl interaction with ILE530 (Fig. 21).

For the docking with chitin synthase of Aspergillus Niger (-4.7 kcal mol^{-1}) it is observed conventional hydrogen bond interaction between THR60 (2.82 and 1.82 Å) and both hydrogen atoms from pirrolic nitrogens of pirazole rings of [$ZnCl_2(\eta^1$-4BrPz$)_2$], it is also observed carbon hydrogen bond with THR58 (3.59 Å), π–sigma SER62, π–lone pair with ASN57 and alkyl interaction with ILE114 (Fig. 22).

The docking with chitin synthase of Candida albicans (-4.1 kcal mol^{-1}) shows hydrogen bond interactions that stabilizes the protein-ligand interaction. Thus it is shown conventional hydrogen bond interactions with GLU16 (2.60 Å), π–donor hydrogen bond with SER21 (2.63 Å), π–alkyl and π–π stacked interactions with PHE17 (Fig. 22).

The evaluation of the absorption, distribution, metabolism and elimination (ADME) processes for [$ZnCl_2(\eta^1$-4BrPz$)_2$] has been performed by using SwissADME webserver.[REF subjected to SwissADME webserver.[68] Thus, Fig. 23 shows the bioavailability and ADME Boiled-Egg model for [$ZnCl_2(\eta^1$-4BrPz$)_2$]. In Fig. 23A the orange zone shows the suitable physicochemical space for oral bioavailability and [$ZnCl_2(\eta^1$-4BrPz$)_2$] compound is located on it based on lipophilicity, flexibility, saturation, size, polarity and solubility factors. It is also found that the compound satisfy both the Lipinski rule of 5 and Veber, that are relevant parameters in drug discovery studies.[69,70] It presents a reasonable synthetic accessibility, with a value 4.25 from 1 (easy) to 10 (very difficult).[71] Fig. 23B shows [$ZnCl_2(\eta^1$-4BrPz$)_2$] compound is located inside the white region that is the physicochemical space of molecules with high probability of gastrointestinal absorption.[72] The molecule presents an acceptable bioavailability score of 0.55 and did not return any pan-assay interference compounds (PAINS) alert. The molecule is found not to be substrate of the permeability glycoprotein (P-gp) so it can act as substrates to other plasmatic transporter protein. It was found not to be inhibitor of cytochromes P450 (CYP) CYP1A2, CYP2C19, CYP2C9, CYP2D6, CYP3A4 key in drugs metabolism and its elimination avoiding adverse effects due to accumulation of the drug or its metabolites.[68]

3.7. Zinc-based organometallic halide and bacteria pathogens

The zinc-based organometallic halide [$ZnCl_2(\eta^1$-4BrPz$)_2$] exhibited a clear concentration-dependent antibacterial effect against all eight tested bacterial strains, encompassing both Gram-positive and Gram-negative species. The size of the inhibition zones increased with concentration, ranging from 3.9–6.3 mm at 0.5 μg mL^{-1} to 14.7–16.8 mm at 2 μg mL^{-1}. As expected, tetracycline (1 μg mL^{-1}) produced larger inhibition zones overall (6.6–22.8 mm), reflecting its well-established antibacterial potency. Nevertheless, the studied compound showed appreciable activity against relatively resistant strains such as *Pseudomonas aeruginosa* and *Micrococcus luteus*, suggesting its potential effectiveness in overcoming partial antibiotic resistance. In addition, moderate inhibitory effects were observed for *Bacillus cereus* and *Salmonella typhi*, indicating a broad-spectrum antibacterial profile.

The observed antimicrobial activity can be attributed to the coordination environment of the zinc center, where its interaction with organic ligands enhances its ability to interact with bacterial cells. The release of Zn^{2+} ions from the complex may disrupt key enzymatic processes, particularly those associated with DNA replication and cellular energy metabolism, ultimately leading to metabolic imbalance.[73–76] Furthermore, the positively charged zinc species can interact electrostatically with negatively charged components of bacterial membranes, increasing membrane permeability and promoting leakage of intracellular contents, which contributes to cell death. The production of reactive oxygen species (ROS), as reported for similar zinc-based systems, may also play a role by inducing oxidative damage to essential biomolecules such as lipids, proteins, and nucleic acids.[31,77–79] Fig. 24 presents the antimicrobial activity of tetracycline against bacterial, fungal, and yeast strains.

This multi-target mechanism provides a distinct advantage over conventional antibiotics, which typically act on a single target, making it harder for bacteria to develop resistance. Moreover, the coordination framework of the zinc center allows for structural modifications, such as tuning the ligand set or coordination geometry, to control zinc release and enhance antibacterial efficacy while minimizing toxicity toward human cells. The observed activity against partially resistant strains underscores the potential of [$ZnCl_2(\eta^1$-4BrPz$)_2$] as a promising alternative or adjunct to standard antibiotics like tetracycline. These results support further investigation into zinc-based organic halides as novel antimicrobial agents and highlight their importance in addressing the growing challenge of antibiotic-resistant bacterial infections.

Regarding the MIC and MBC values of the [$ZnCl_2(\eta^1$-4BrPz$)_2$] complex and its free ligand (4BrP), our results, as shown in Table S7, demonstrate that [$ZnCl_2(\eta^1$-4BrPz$)_2$] exhibits significantly stronger antibacterial activity than the ligand alone. MIC values for the complex ranged from 0.45 to 2.10 μg mL^{-1}, while those of the free ligand were much higher, between 2.89 and 7.84 μg mL^{-1}. Similarly, MBC values for the complex (0.87–3.74 μg mL^{-1}) were considerably lower than those of the ligand (11.7–19.76 μg mL^{-1}). The MBC/MIC ratios of the complex (1.41–2.01) indicate a strong bactericidal effect against all tested strains, whereas the ligand alone showed ratios between 2.52 and 4.54, suggesting weak to moderate bactericidal activity. Among the tested strains, *Escherichia coli* and *Bacillus cereus* were the most sensitive to the complex, while *Pseudomonas aeruginosa* and *Salmonella typhi* exhibited slightly lower sensitivity, likely due to intrinsic resistance mechanisms such as efflux pumps or reduced membrane permeability. The superior activity of [$ZnCl_2(\eta^1$-4BrPz$)_2$] compared to the ligand highlights the critical role of metal–ligand coordination. This enhanced effect may result from multiple synergistic mechanisms, including coordination of zinc ions to bacterial enzymes, disruption of the bacterial cell membrane by the complex, and induction of oxidative stress, leading to DNA and membrane damage.

Our results indicate that $[ZnCl_2(\eta^1\text{-}4BrPz)_2]$ and its free ligand exhibited no acute toxicity. Throughout the treatment period, the rats showed no behavioral changes, weight loss, or digestive disturbances. Furthermore, biochemical analyses revealed no significant alterations in blood glucose, hepatic enzymes (AST and ALT), or renal markers (creatinine and urea) compared to control animals. These findings confirm that both the complex and the free ligand are well tolerated at the tested doses, indicating a favorable safety profile for subsequent therapeutic tests.

4 Conclusion

In this work, we report the synthesis and comprehensive characterization of the zinc-based coordination halide $[ZnCl_2(\eta^1\text{-}4BrPz)_2]$ through experimental crystallography, spectroscopy, thermal analysis, and computational studies, complemented by biological evaluation. Single-crystal X-ray diffraction reveals an uncommon asymmetric arrangement with two crystallographically distinct Zn(II) tetrahedra, stabilized by a network of non-covalent interactions. Hirshfeld surface, ELF, and NCI analyses highlight the key roles of Br···Br, Br···Cl, π···π stacking, and hydrogen-assisted contacts in reinforcing the three-dimensional crystal structure. Thermal analyses confirm the compound's high structural robustness, while periodic DFT calculations provide a consistent electronic and bonding description, rationalizing the observed stability and organization. Beyond its structural features, $[ZnCl_2(\eta^1\text{-}4BrPz)_2]$ exhibits promising biological potential: molecular docking predicts favorable binding to bacterial DNA gyrase and fungal chitin synthase, supported by hydrogen-bonding, halogen-assisted, and π-mediated interactions, which are confirmed by *in vitro* antibacterial assays. Overall, the study demonstrates how brominated ligands enhance crystal stability, electronic coherence, and biological activity, providing design principles for multifunctional zinc-based coordination materials.

Author contributions

Houyem Khlifi: formal analysis, writing–original draft; Naoufel Ben Hamadi: formal analysis, investigation; Noureddine Mhadbi: data curation, investigation; Antonio Sánchez-Coronilla: data curation, investigation; Khaled Hamden: formal analysis, validation; Ahlem Guesmi: formal analysis, software; Lotfi Khezami: data curation, investigation; Hajir Wahbi: investigation, validation; Houcine Naïli: project administration, review & editing.

Conflicts of interest

The authors declare that they have no known competing financial interests or personal relationships that could have appeared to influence the work reported in this paper.

Data availability

The data that supported the findings of this study were available upon reasonable request.

Supplementary information (SI): crystallographic data, computational analyses, molecular docking, spectroscopic characterization, and antimicrobial studies of the zinc(II) complex $[ZnCl_2(\eta^1\text{-}4BrPz)_2]$. See DOI: https://doi.org/10.1039/d6ra01123c.

CCDC 2541470 contains the supplementary crystallographic data for this paper.[80]

Acknowledgements

This work was supported and funded by the Deanship of Scientific Research at Imam Mohammad Ibn Saud Islamic University (IMSIU) (grant number IMSIU-DDRSP2603).

References

1 T. Zhang, H. Li, P. Yang, J. Wei, F. Wang, H. Shen, D. Li and F. Li, Room-temperature synthesized formamidinium lead halide perovskite quantum dots with bright luminescence and color-tunability for efficient light emitting, *Org. Electron.*, 2019, **68**, 76–84, DOI: 10.1016/j.orgel.2019.02.007.

2 C. Zhao, Z. Zhou, M. Almalki, M. A. Hope, J. Zhao, T. Gallet, A. Krishna, A. Mishra, F. T. Eickemeyer, J. Xu, Y. Yang, S. M. Zakeeruddin, A. Redinger, T. J. Savenije, L. Emsley, J. Yao, H. Zhang and M. Grätzel, Stabilization of highly efficient perovskite solar cells with a tailored supramolecular interface, *Nat. Commun.*, 2024, **15**, 7139, DOI: 10.1038/s41467-024-51550-z.

3 Y. Du, J. Wu, X. Zhang, Q. Zhu, M. Zhang, X. Liu, Y. Zou, S. Wang and W. Sun, Surface passivation using pyridinium iodide for highly efficient planar perovskite solar cells, *J. Energy Chem.*, 2021, **52**, 84–91, DOI: 10.1016/j.jechem.2020.04.049.

4 S. Pang, H. Hu, J. Zhang, S. Lv, Y. Yu, F. Wei, T. Qin, H. Xu, Z. Liu and G. Cui, NH 2 CH=NH 2 PbI 3 : An Alternative Organolead Iodide Perovskite Sensitizer for Mesoscopic Solar Cells, *Chem. Mater.*, 2014, **26**, 1485–1491, DOI: 10.1021/cm404006p.

5 T. Qiu, Y. Hu, F. Xu, Z. Yan, F. Bai, G. Jia and S. Zhang, Recent advances in one-dimensional halide perovskites for optoelectronic applications, *Nanoscale*, 2018, **10**, 20963–20989, DOI: 10.1039/C8NR05862H.

6 A. Wang, C. Zuo, X. Niu, L. Ding, J. Ding and F. Hao, Recent promise of lead-free halide perovskites in optoelectronic applications, *Chem. Eng. J.*, 2023, **451**, 138926, DOI: 10.1016/j.cej.2022.138926.

7 H. J. Snaith, Perovskites: The Emergence of a New Era for Low-Cost, High-Efficiency Solar Cells, *J. Phys. Chem. Lett.*, 2013, **4**, 3623–3630, DOI: 10.1021/jz4020162.

8 B. Saparov and D. B. Mitzi, Organic–Inorganic Perovskites: Structural Versatility for Functional Materials Design, *Chem. Rev.*, 2016, **116**, 4558–4596, DOI: 10.1021/acs.chemrev.5b00715.

9 G. Lozano, The Role of Metal Halide Perovskites in Next-Generation Lighting Devices, *J. Phys. Chem. Lett.*, 2018, **9**, 3987–3997, DOI: 10.1021/acs.jpclett.8b01417.
10 C. Quarti, N. Marchal and D. Beljonne, Tuning the Optoelectronic Properties of Two-Dimensional Hybrid Perovskite Semiconductors with Alkyl Chain Spacers, *J. Phys. Chem. Lett.*, 2018, **9**, 3416–3424, DOI: 10.1021/acs.jpclett.8b01309.
11 J.-P. Correa-Baena, A. Abate, M. Saliba, W. Tress, T. Jesper Jacobsson, M. Grätzel and A. Hagfeldt, The rapid evolution of highly efficient perovskite solar cells, *Energy Environ. Sci.*, 2017, **10**, 710–727, DOI: 10.1039/C6EE03397K.
12 J. Even, L. Pedesseau, J.-M. Jancu and C. Katan, Importance of Spin–Orbit Coupling in Hybrid Organic/Inorganic Perovskites for Photovoltaic Applications, *J. Phys. Chem. Lett.*, 2013, **4**, 2999–3005, DOI: 10.1021/jz401532q.
13 A. Kojima, K. Teshima, Y. Shirai and T. Miyasaka, Organometal Halide Perovskites as Visible-Light Sensitizers for Photovoltaic Cells, *J. Am. Chem. Soc.*, 2009, **131**, 6050–6051, DOI: 10.1021/ja809598r.
14 T. Baikie, Y. Fang, J. M. Kadro, M. Schreyer, F. Wei, S. G. Mhaisalkar, M. Graetzel and T. J. White, Synthesis and crystal chemistry of the hybrid perovskite (CH3NH3) PbI3 for solid-state sensitised solar cell applications, *J. Mater. Chem. A*, 2013, **1**, 5628, DOI: 10.1039/c3ta10518k.
15 T. K. Todorov, D. M. Bishop and Y. S. Lee, Materials perspectives for next-generation low-cost tandem solar cells, *Sol. Energy Mater. Sol. Cells*, 2018, **180**, 350–357, DOI: 10.1016/j.solmat.2017.07.033.
16 K. J. Savill, A. M. Ulatowski and L. M. Herz, Optoelectronic Properties of Tin–Lead Halide Perovskites, *ACS Energy Lett.*, 2021, **6**, 2413–2426, DOI: 10.1021/acsenergylett.1c00776.
17 D. Pal and S. Das, Numerical modeling and simulation for augmenting the photovoltaic response of HTL free perovskite solar cells, Mater, *Today Proc.*, 2021, **46**, 6367–6373, DOI: 10.1016/j.matpr.2020.05.826.
18 H. Dong, C. Ran, W. Gao, M. Li, Y. Xia and W. Huang, Metal Halide Perovskite for next-generation optoelectronics: progresses and prospects, *ELight*, 2023, **3**, 3, DOI: 10.1186/s43593-022-00033-z.
19 B. Diouf, A. Muley and R. Pode, Issues, Challenges, and Future Perspectives of Perovskites for Energy Conversion Applications, *Energies*, 2023, **16**, 6498, DOI: 10.3390/en16186498.
20 D. V. Amasev, A. R. Tameev and A. G. Kazanskii, Features of the Temperature Dependences of the Photoconductivity of Organometallic CH3NH3PbI3 Perovskite Films, *Semiconductors*, 2019, **53**, 1597–1602, DOI: 10.1134/S1063782619160024.
21 A. Aziz, N. Aristidou, X. Bu, R. J. E. Westbrook, S. A. Haque and M. S. Islam, Understanding the Enhanced Stability of Bromide Substitution in Lead Iodide Perovskites, *Chem. Mater.*, 2020, **32**, 400–409, DOI: 10.1021/acs.chemmater.9b04000.
22 H. Wang, X. Wang, H. Zhang, W. Ma, L. Wang and X. Zong, Organic−inorganic hybrid perovskites: Game-changing candidates for solar fuel production, *Nano Energy*, 2020, **71**, 104647, DOI: 10.1016/j.nanoen.2020.104647.
23 C. Park, S. J. Yang, J. Choi, S. Song, W. Choi and K. Cho, Improved Chemical Stability of Organometal Halide Perovskite Solar Cells Against Moisture and Heat by Ag Doping, *ChemSusChem*, 2020, **13**, 3261–3268, DOI: 10.1002/cssc.202000192.
24 S. Mohammad, E. Rahman and A. Rahman, Science of the Total Environment Exploring agro-waste derived inorganic nanoparticles (Ag , ZnO , and SiO2) in the food industry : Green synthesis , characteristics , and applications – A comprehensive review, *Sci. Total Environ.*, 2025, **1008**, 181009, DOI: 10.1016/j.scitotenv.2025.181009.
25 A. M. Mohammed, M. Mohammed, J. K. Oleiwi, F. H. Ihmedee, T. Adam, B. O. Betar and S. C. B. Gopinath, Nano Trends Comprehensive review on zinc oxide nanoparticle production and the associated antibacterial mechanisms and therapeutic potential, *Nano Trends*, 2025, **11**, 100145, DOI: 10.1016/j.nwnano.2025.100145.
26 S. S. Ali, R. Al-tohamy and J. Sun, Environmental Chemistry and Ecotoxicology Disruptive technology for integrating bioremediation and biodiesel production from persistent toxic aromatic wastes using termite gut yeasts, *Environ. Chem. Ecotoxicol.*, 2025, **7**, 462–493, DOI: 10.1016/j.enceco.2025.02.005.
27 M. Sobhy, T. Elsamahy, E. A. Abdelkarim, E. Khojah, H. Cui and L. Lin, Microbial Pathogenesis Cardamom essential oil-loaded zinc oxide nanoparticles : A sustainable antimicrobial strategy against multidrug-resistant foodborne pathogens, *Microb. Pathog.*, 2025, **205**, 107661, DOI: 10.1016/j.micpath.2025.107661.
28 T. Xu, G. Li, M. Du and J. Wang, Bioelectrochemistry Study on inhibition of sulfate-reducing bacteria corrosion by synergistic action of corrosion inhibitors and biological mineralization, *Bioelectrochemistry*, 2025, **166**, 109056, DOI: 10.1016/j.bioelechem.2025.109056.
29 Z. Zhang, J. Li, C. Wang, Q. Ren and R. Zhang, Synthesis of near infrared absorbing cationic zinc aminophthalocyanine and its application as an efficient photo-sensitizing nanoparticle in anti-drug-resistant bacteria, *Synth. Met.*, 2023, **296**, 117377, DOI: 10.1016/j.synthmet.2023.117377.
30 R. Gnanasekaran, D. Yuvaraj, G. K. Reddy, S. N. Shangar, V. Vijayakumar and J. Iyyappan, Environmental Chemistry and Ecotoxicology Zinc oxide nanoparticles from leaf extract of Eclipta prostrata : Biosynthesis and characterization towards potential agent against film forming bacteria in metal working fluids, *Environ. Chem. Ecotoxicol.*, 2024, **6**, 206–215, DOI: 10.1016/j.enceco.2024.06.001.
31 Y. Liu, Q. Ma, L. Tang, Y. Shen, H. Zhao, X. Liu and D. Lin, A multifunctional hydrogel with mild photothermal antibacterial and antioxidant properties based on quercetin and dopamine-coated zinc oxide nanoparticles for healing bacteria-infected wound, *Chem. Eng. J.*, 2024, **497**, 154518, DOI: 10.1016/j.cej.2024.154518.

32 *Rigaku Oxford Diffraction, CrysAlisPro Software System, Version 1.171.41.93a*, Rigaku Corporation, Oxford, UK, 2020.
33 Bruker AXS Inc., *SAINT, Version 8.38A*, Bruker AXS Inc., Madison, Wisconsin, USA, 2015.
34 Bruker AXS Inc., *SADABS, Version 2016/2*, Bruker AXS Inc., Madison, Wisconsin, USA, 2016.
35 L. J. Farrugia, WinGX and ORTEP for Windows: an update, *J. Appl. Crystallogr.*, 2012, **45**, 849–854, DOI: 10.1107/S0021889812029111.
36 G. M. Sheldrick, SHELXT – Integrated space-group and crystal-structure determination, Acta Crystallogr. A Found, *Adv*, 2015, **71**, 3–8, DOI: 10.1107/S2053273314026370.
37 G. M. Sheldrick, Crystal structure refinement with SHELXL, *Acta Crystallogr., Sect. C:Struct. Chem.*, 2015, **71**, 3–8, DOI: 10.1107/S2053229614024218.
38 K. Brandenburg and H. Putz, *DIAMOND – Crystal and Molecular Structure Visualization*, Crystal Impact GbR, Bonn, Germany, 2005.
39 M. Ashfaq, M. Nawaz Tahir, K. S. Munawar, R. Behjatmanesh-Ardakani and H. Kargar, Single crystal exploration, supramolecular behaviour, Hirshfeld surface analysis, linear and non-linear theoretical optical properties of Schiff bases derived from Benzene sulfonamides, *J. Mol. Struct.*, 2022, **1261**, 132952, DOI: 10.1016/j.molstruc.2022.132952.
40 H. Kargar, A. A. Ardakani, M. N. Tahir, M. Ashfaq and K. S. Munawar, Synthesis, spectral characterization, crystal structure and antibacterial activity of nickel(II), copper(II) and zinc(II) complexes containing ONNO donor Schiff base ligands, *J. Mol. Struct.*, 2021, **1233**, 130112, DOI: 10.1016/j.molstruc.2021.130112.
41 M. Ashfaq, A. Ali, M. N. Tahir, A. Kuznetsov, K. S. Munawar and S. Muhammad, Synthesis, single-crystal exploration, hirshfeld surface analysis, and DFT investigation of the thiosemicarbazones, *J. Mol. Struct.*, 2022, **1262**, 133088, DOI: 10.1016/j.molstruc.2022.133088.
42 M. Haroon, T. Akhtar, M. Yousuf, M. N. Tahir, L. Rasheed, S. S. Zahra, I. ul Haq and M. Ashfaq, Synthesis, crystal structure, Hirshfeld surface investigation and comparative DFT studies of ethyl 2-[2-(2-nitrobenzylidene)hydrazinyl] thiazole-4-carboxylate, *BMC Chem.*, 2022, **16**, 18, DOI: 10.1186/s13065-022-00805-1.
43 S. S. Hasanova, L. N. Mamedova, M. Ashfaq, K. S. Munawar, E. M. Movsumov, M. Khalid, M. N. Tahir and M. Imran, Synthesis, crystal structure, Hirshfeld surface analysis and theoretical investigation of polynuclear coordination polymers of cobalt and manganese complexes with nitrobenzene and pyrazine, *J. Mol. Struct.*, 2022, **1250**, 131851, DOI: 10.1016/j.molstruc.2021.131851.
44 A. M. Maharramov, G. S. Duruskari, G. Z. Mammadova, A. N. Khalilov, J. M. Aslanova, J. Cisterna, A. Cárdenas and I. Brito, Crystal Structure And Hirshfeld Surface Analysis Of (E)-5-Phenyl-3-((4-(Trifluoromethyl)Benzylidene)Amino) Thiazolidin-2-Iminium Bromide, *J. Chil. Chem. Soc.*, 2019, **64**, 4441–4447, DOI: 10.4067/S0717-97072019000204441.
45 G. Nandini and Ds Sathyanarayana, Ab initio studies on molecular conformation and vibrational spectra of propionamide, *J. Mol. Struct.:THEOCHEM*, 2002, **586**, 125–135, DOI: 10.1016/S0166-1280(02)00079-9.
46 P. E. Blöchl, O. Jepsen and O. K. Andersen, Improved tetrahedron method for Brillouin-zone integrations, *Phys. Rev. B*, 1994, **49**, 16223–16233, DOI: 10.1103/PhysRevB.49.16223.
47 G. Kresse and J. Furthmüller, Efficiency of ab-initio total energy calculations for metals and semiconductors using a plane-wave basis set, *Comput. Mater. Sci.*, 1996, **6**, 15–50, DOI: 10.1016/0927-0256(96)00008-0.
48 G. Kresse and J. Furthmüller, Efficient iterative schemes for ab initio total-energy calculations using a plane-wave basis set, *Phys. Rev. B*, 1996, **54**, 11169–11186, DOI: 10.1103/PhysRevB.54.11169.
49 G. Kresse and J. Hafner, Ab initio molecular dynamics for liquid metals, *Phys. Rev. B*, 1993, **47**, 558–561, DOI: 10.1103/PhysRevB.47.558.
50 G. Kresse and J. Hafner, Ab initio molecular-dynamics simulation of the liquid-metal–amorphous-semiconductor transition in germanium, *Phys. Rev. B*, 1994, **49**, 14251–14269, DOI: 10.1103/PhysRevB.49.14251.
51 A. D. Becke, Density-functional thermochemistry. III. The role of exact exchange, *J. Chem. Phys.*, 1993, **98**, 5648–5652, DOI: 10.1063/1.464913.
52 A. D. Becke and K. E. Edgecombe, A simple measure of electron localization in atomic and molecular systems, *J. Chem. Phys.*, 1990, **92**, 5397–5403, DOI: 10.1063/1.458517.
53 J. P. Perdew, K. Burke and M. Ernzerhof, Generalized Gradient Approximation Made Simple, *Phys. Rev. Lett.*, 1996, **77**, 3865–3868, DOI: 10.1103/PhysRevLett.77.3865.
54 G. Hossein Shafiee, Conformational and Bonding Analysis of C& lt;sub& gt;2& lt;/sub& gt;H& lt;sub& gt;4& lt;/sub& gt;& lt;sup& gt;2+& lt;/sup& gt, *Open J. Phys. Chem.*, 2012, **02**, 176–181, DOI: 10.4236/ojpc.2012.23023.
55 T. B. Terriberry, D. F. Cox and D. A. Bowman, A tool for the interactive 3D visualization of electronic structure in molecules and solids, *Comput. Chem.*, 2002, **26**, 313–319, DOI: 10.1016/S0097-8485(01)00120-6.
56 A. Otero-de-la-Roza, M. A. Blanco, A. M. Pendás and V. Luaña, Critic: a new program for the topological analysis of solid-state electron densities, *Comput. Phys. Commun.*, 2009, **180**, 157–166, DOI: 10.1016/j.cpc.2008.07.018.
57 A. Otero-de-la-Roza, E. R. Johnson and V. Luaña, Critic2: A program for real-space analysis of quantum chemical interactions in solids, *Comput. Phys. Commun.*, 2014, **185**, 1007–1018, DOI: 10.1016/j.cpc.2013.10.026.
58 W. Humphrey, A. Dalke and K. Schulten, VMD: Visual molecular dynamics, *J. Mol. Graph.*, 1996, **14**, 33–38, DOI: 10.1016/0263-7855(96)00018-5.
59 M. A. Matin, M. M. Islam, T. Bredow and M. A. Aziz, The Effects of Oxidation States, Spin States and Solvents on Molecular Structure, Stability and Spectroscopic Properties of Fe-Catechol Complexes: A Theoretical Study, *Adv. Chem. Eng. Sci.*, 2017, **07**, 137–153, DOI: 10.4236/aces.2017.72011.
60 A. Waterhouse, M. Bertoni, S. Bienert, G. Studer, G. Tauriello, R. Gumienny, F. T. Heer, T. A. P. de Beer,

C. Rempfer, L. Bordoli, R. Lepore and T. Schwede, SWISS-MODEL: homology modelling of protein structures and complexes, *Nucleic Acids Res.*, 2018, **46**, W296–W303, DOI: 10.1093/nar/gky427.

61 R. A. Laskowski, J. D. Watson and J. M. Thornton, ProFunc: a server for predicting protein function from 3D structure, *Nucleic Acids Res.*, 2005, **33**, W89–W93, DOI: 10.1093/nar/gki414.

62 O. Trott and A. J. Olson, AutoDock Vina: Improving the speed and accuracy of docking with a new scoring function, efficient optimization, and multithreading, *J. Comput. Chem.*, 2010, **31**, 455–461, DOI: 10.1002/jcc.21334.

63 G. M. Morris, R. Huey, W. Lindstrom, M. F. Sanner, R. K. Belew, D. S. Goodsell and A. J. Olson, AutoDock4 and AutoDockTools4: Automated docking with selective receptor flexibility, *J. Comput. Chem.*, 2009, **30**, 2785–2791, DOI: 10.1002/jcc.21256.

64 S. Hossain, B. Sarkar, M. N. I. Prottoy, Y. Araf, M. A. Taniya and M. A. Ullah, Thrombolytic Activity, Drug Likeness Property and ADME/T Analysis of Isolated Phytochemicals from Ginger (& lt;i& gt;Zingiber officinale& lt;/i& gt;) Using & lt;i& gt;In Silico& lt;/i& gt; Approaches, *Mod. Res. Inflamm.*, 2019, **08**, 29–43, DOI: 10.4236/mri.2019.83003.

65 K. Meszaros, V. M. Leovac, Ž. K. Jacimovic, V. I. Češljevic, A. Kovacs, G. Pokol and S. Gal, Transition metal complexes with pyrazole-based ligands. Part 8. Characterization and thermal decomposition of zinc“II” complexes with di- and trisubstituted pyrazoles, *J. Therm. Anal. Calorim.*, 2001, **63**, 723–732, DOI: 10.1023/A:1010135903480.

66 N. A. Peterson and M. A. Zimmerman, Beyond the individual: toward a nomological network of organizational empowerment, *Am. J. Community Psychol.*, 2004, **34**, 129–145, DOI: 10.1023/B:AJCP.0000040151.77047.58.N.

67 S. Zairi, N. Ben Hamadi, H. Elleuch, H. Khlifi, S. Walha, A. Ben Ahmed, H. Wahbi, A. Guesmi, L. Khezami, F. Rezgui, A. Sanchez-Coronilla and H. Naïli, Synthesis, crystal structure, DFT analysis, and multifunctional biological activity of a new organotin(IV) phosphonate complex, *Polyhedron*, 2026, **291**, 118086, DOI: 10.1016/j.poly.2026.118086.

68 A. Daina, O. Michielin and V. Zoete, SwissADME: a free web tool to evaluate pharmacokinetics, drug-likeness and medicinal chemistry friendliness of small molecules, *Sci. Rep.*, 2017, **7**, 42717, DOI: 10.1038/srep42717.

69 R. Bhagat and R. Saudagar, Osteoarthritis: pathophysiology and current treatment modalitiesJ. Drug Delivery Ther., *Ther.*, 2019, **9**, 661–668, DOI: 10.22270/jddt.v9i3.2678.

70 M. Kowalska, Ł. Fijałkowski and A. Nowaczyk, The biological activity assessment of potential drugs acting on cardiovascular system using Lipinski and Veber Rules, *J. Educ.*, 2018, **8**, 2391–8306, DOI: 10.5281/zenodo.2066519.

71 P. Ertl and A. Schuffenhauer, Estimation of synthetic accessibility score of drug-like molecules based on molecular complexity and fragment contributions, *J. Cheminform.*, 2009, **1**, 8, DOI: 10.1186/1758-2946-1-8.

72 A. Daina and V. Zoete, A BOILED-Egg To Predict Gastrointestinal Absorption and Brain Penetration of Small Molecules, *ChemMedChem*, 2016, **11**, 1117–1121, DOI: 10.1002/cmdc.201600182.

73 J. Nan, Y. Chu, R. Guo and P. Chen, Research on the antibacterial properties of nanoscale zinc oxide particles: comprehensive review, *Front. Mater.*, 2024, **11**, 1449614, DOI: 10.3389/fmats.2024.1449614.

74 Y. Hao, Y. Wang, L. Zhang, F. Liu, Y. Jin, J. Long, S. Chen, G. Duan and H. Yang, Advances in antibacterial activity of zinc oxide nanoparticles against Staphylococcus aureus (Review), *Biomed. Rep*, 2024, **21**, 161, DOI: 10.3892/br.2024.1849.

75 A. R. Mendes, C. M. Granadeiro, A. Leite, E. Pereira, P. Teixeira and F. Poças, Optimizing antimicrobial efficacy: investigating the impact of zinc oxide nanoparticle shape and size, *Nanomaterials*, 2024, **14**, 638, DOI: 10.3390/nano14070638.

76 E. L. Irede, R. F. Awoyemi, B. Owolabi, O. R. Aworinde, R. O. Kajola, A. Hazeez, A. A. Raji, L. O. Ganiyu, C. O. Onukwuli, A. P. Onivefu and I. H. Ifijen, Cutting-edge developments in zinc oxide nanoparticles: synthesis and applications for enhanced antimicrobial and UV protection in healthcare solutions, *RSC Adv.*, 2024, **14**, 20992–21034, DOI: 10.1039/D4RA02452D.

77 R. Acharya, F. Tettey and A. Gupta, Bioinspired synthesis and characterization of zinc oxide nanoparticles and assessment of their cytotoxicity and antimicrobial efficacy, *Discover Appl. Sci.*, 2024, **6**, 85, DOI: 10.1007/s42452-024-05719-2.

78 A. T. Reda, J. Y. Park and Y. T. Park, Zinc oxide-based nanomaterials for microbiostatic activities: a review, *J. Funct. Biomater.*, 2024, **15**, 103, DOI: 10.3390/jfb15040103.

79 H. Jiang, L. Li, Z. Li and X. Chu, Metal-based nanoparticles in antibacterial application in biomedical field: current development and potential mechanisms, *Biomed. Microdevices*, 2024, **26**, 12, DOI: 10.1007/s10544-023-00686-8.

80 CCDC 2541470: Experimental Crystal Structure Determination, 2026, DOI: 10.5517/ccdc.csd.cc2r9lxl.